Axonal tree morphology and signal propagation dynamics improve neuronal classification

Netanel Ofer[1,2], Orit Shefi[1,2,*], and Gur Yaari[1,*]

[1]Faculty of Engineering, Bar Ilan University, Ramat Gan 5290002, Israel.
[2]Bar Ilan Institute of Nanotechnologies and Advanced Materials, Bar Ilan University, Ramat Gan 5290002, Israel.

Abstract

Classification of neurons into specific subtypes is essential for better understanding of brain function and information transmission. Despite continuous progress, there is still no consensus regarding categorizing neuron taxonomy into proper subtypes. Current morphology-based classification approaches largely rely on the dendritic tree structure or on the general axonal projection layout. In this study, we support the use of a morphology-based classification approach, focusing on the axonal tree. We demonstrate that utilizing the geometrical parameters of axonal tree structures significantly improves neuronal classification compared to the dendritic tree classification. Furthermore, we used neuronal activity patterns to classify interneurons into subtypes as well. Simulations of the activity along ramified axonal trees indicate that the axonal branching geometry may yield diverse responses in different subtrees. The classification schemes introduced here can be utilized to robustly classify neuronal subtypes in a functionally relevant manner. Our results open the door for deducing functionality from anatomical data.

Quantitative analysis of neuronal types and their properties are critical for better understanding and deciphering brain function[1–3]. Despite the attempts to standardize the terminology for neuronal types, there is no clear consensus regarding neuron nomenclature[4], leaving neuronal classification an ongoing challenge[5–11]. To date, interneuron classification is based on morphology[12], membrane properties and firing patterns[13–15], neurochemical markers[16,17], connectivity patterns[18,19], transcriptome[20–24], and epigenomics[25]. The resulting classifications are highly correlated, implying that these subtypes indicate functionally distinct classes[26–31]. The morphology-based classification approaches include dendritic tree geometry[32–35] and axonal projection[36–38], where directionalities of axons are taken into account. Topological persistence-based methods were also developed to support comparisons between individual neurons and classification[39–42]. Topological motifs of the axonal tree were found to differentiate interneurons and pyramidal cells[43–45]. So far, no studies have used the geometrical properties of the axonal tree for neuronal classification, specifically the axonal branch diameter, branch length, and the geometric ratio (GR) values.

Different types of neurons have different ion channels with various kinematics and densities, spreading across the soma, axons and dendrites[46,47]. Using evolutionary algorithms, the *Blue Brain Project* (BBP) fitted the experimental recordings of rat cortical neurons with specific ion channel types and parameters[48,49]. Firing patterns are commonly defined by neuronal responses to step currents, according to the criteria established at the Petilla convention[50]. Combinations of continuous, delayed, and bursting onset patterns, with accommodating, non-accommodating, stuttering, irregular, and adapting steady-state behaviors, led to establishing eleven electrical types (e-types), ten of which exist in interneurons and one in pyramidal cells. The distribution of each of the ion channels along specific neuronal types and cortical layers as well as the fitted parameters are indicated

in the Neocortical Microcircuit Collaboration Portal (NMC)[51]. Activity-based neuronal classification is a promising and interesting path that remains to be explored.

Here, we have leveraged the advancement of imaging techniques that led to growth in high-resolution 3D reconstructions along with the development of big neuronal morphology databases, such as the *Blue Brain Project*[52], the *Allen Institute Brain Atlas*[53,54], and *NeuroMorpho.Org*[55] to classify neurons into subtypes based on their morphology and activity. We first classified interneurons based on axonal tree morphology parameters, obtaining fairly accurate discrimination. Adding dendritic tree morphology to the axonal one improved the prediction rates. Finally, we considered an axonal tree activity-based neuronal classification and further improved the classification's results. Building a classification scheme based on all these features is shown here to robustly classify neurons in a functionally relevant manner.

Results

Classification of interneuron types by morphology

To classify interneurons based on axonal tree morphologies, high-resolution traced neurons were analyzed. For this purpose, neuron reconstructions were downloaded from the *NeuroMorpho.Org* database, and filtered for several criteria to obtain a high-quality dataset for classification (Table 1). Only neurons from a cortex with at least 10 axonal branches and 1,000 axonal segments were included. To achieve high precision in axonal tree geometry, only neurons with at least 10 axonal diameter values measured were included. The resulting filtered dataset is diverse because the interneurons were taken from different cortical layers of male and female rats (n=312, 78%) and mice (n=90, 22%), and were analyzed by different labs. Figure 1 shows representative examples of interneuron morphology types[56]. The distinct geometrical properties of these axonal trees are evident.

Filter criteria	basket	Martinotti	neurogilaform	bitufted	double bouquet	chandelier	bipolar
All data in NeuroMorpho.Org 7.4	829	294	209	93	64	68	606
Cortex only	564	228	139	88	63	36	40
With both axon and dendrite data	508	224	127	56	56	31	40
≥ 10 axonal branches and $\geq 1,000$ axonal segments	437	193	122	53	52	29	34
≥ 10 axonal diameter values measured	196	99	40	20	20	17	10

Table 1: Neuron reconstructions filtration. The table summarizes the number of neurons that were included after each filtration step according to their types.

The most prominent interneuron types are basket, bitufted, chandelier, Martinotti, and neurogliaform[57]. Owing to the wide variety of basket cell morphologies, they are commonly divided into large, nest, and small basket cell subclasses[58]. We therefore focused here on classifying four types of interneurons: bitufted, chandelier, Martinotti, and neurogliaform (see also the Supplementary material for an analysis of all types).

Each neuron reconstruction is characterized by 28 features, based on common quantitative morphological measurements[50,59,60]. The parameters can be divided into three categories: overall topology, branch length, and diameter (Supplementary Table S1). Overall topology measurements include the number of branches, the branch order, Sholl analysis[61], the axonal tree size, and symmetry. Branch length-related parameters include the total length, the branch lengths, the path length, and the branch length divided by the square root of the diameter[62]. The diameter-related parameters include the mean and max diameter values and the GR measures[63]. These features are expected to reflect signal propagation dynamics along the axonal tree[62,64,65].

To avoid biases in classification due to unequal group sizes, we down-sampled our data to include 16 neurons in each group. These neurons were selected as the reconstructions with the highest number of diameter values measured from each group. Briefly, we applied a 4-fold cross validation scheme with 1,000 repeats, and used a multinomial logistic regression approach with regularization to

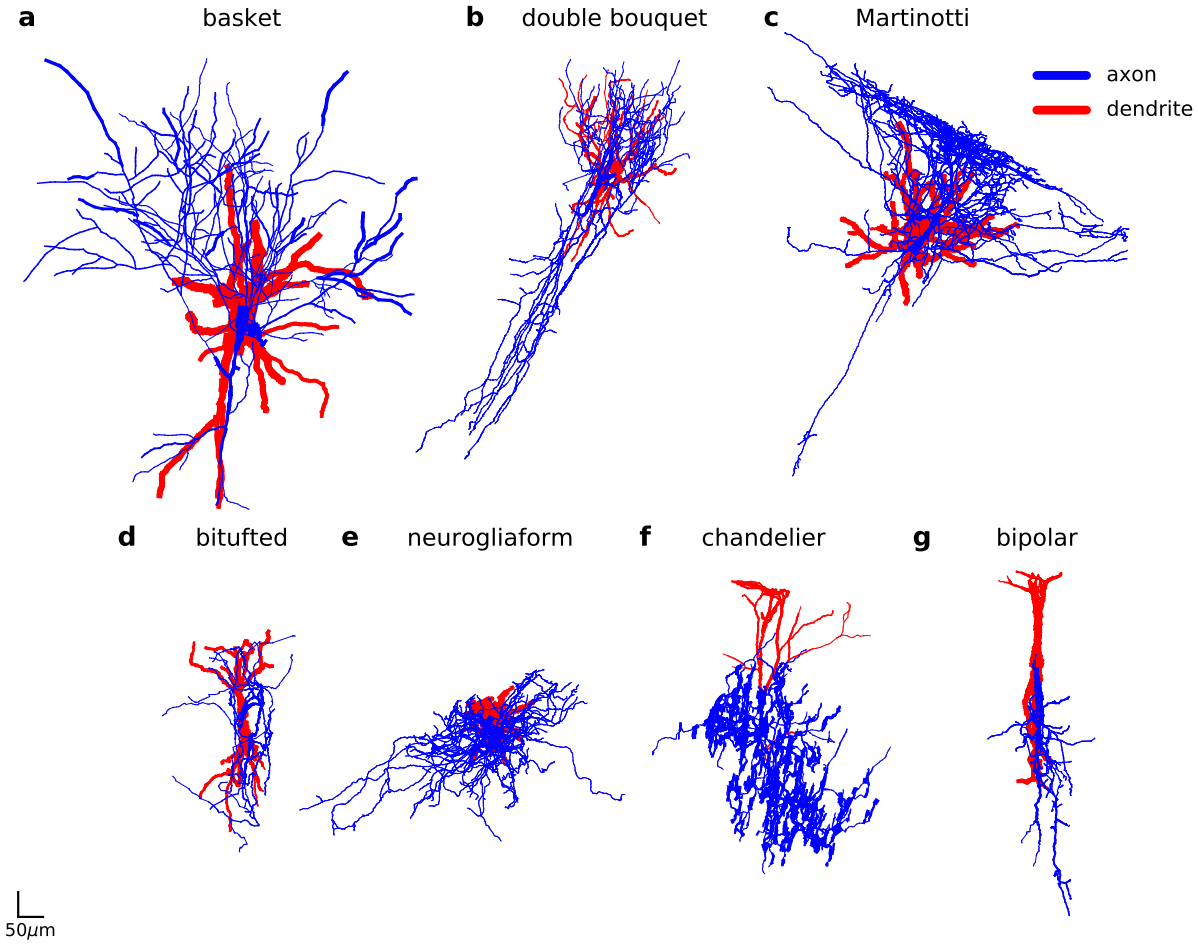

Figure 1: Representative examples of different interneuronal types. Line width is proportional to the axonal (blue) or dendritic (red) segment's corresponding diameter. Data are projected into the XY plane. Cells used for visualizations are as follows: NMO_06143 (**a**), NMO_61613 (**b**), NMO_79459 (**c**), NMO_61580 (**d**), NMO_37062 (**e**), NMO_04548 (**f**), and NMO_61602 (**g**).

classify the data. The resulting F_1-scores are presented in Fig. 2a. F_1-scores range between 0.776, for bitufted cells, and 0.928 for chandelier, resulting in an average F_1-score of 0.837, based only on the axonal tree's morphological parameters. These results are supported by the fact that chandelier cells are, indeed, the easiest cells for experts to classify manually[12]. To validate our approach, we repeated this process for shuffled label data in which we permuted the interneuron type labels among all the cells in the data. This exercise resulted in a significantly lower performance, with an average F_1-score of 0.196 (Supplementary Fig. S1a). To emphasize the importance of the diameter-related measures for this classification, we constructed a distinct data set composed of interneurons with a smaller number of diameter measurement values. In particular, we replaced the 16 interneurons in each group, which were selected according to the *highest* number of diameter values measured, with another selection of 16 interneurons in each group with the *lowest* number of diameter values measured. This new selection of interneurons is included in the fourth row of Table 1 but it is discarded in the fifth row. The resulting average F_1-score is 0.702 (Supplementary Fig. S1b), compared to 0.837 in the high-resolution case. This result supports our assumption that fine diameter differences are important for classifying interneuron types; this may be relevant for enhancing our understanding of the different interneuron types. To further explore this point, we forced all radii in the initial high-resolution data to be $1\mu m$, and performed a similar classification scheme. Interestingly, the average F_1-score decreased from 0.837 to 0.646 (Supplementary Fig. S1c).

To compare the above classification based on axonal tree morphology to the more common classification based on dendritic tree morphology, we applied an analogous classification approach to the

dendritic trees of the *same* neurons. The resulting F_1-scores are presented in Fig. 2b. The dendritic tree-based classification is better for detecting neurogliaform cells (0.83 compared to 0.445-0.623 in other cell types). This result agrees with the observation that neurogliaform cells are known for their thinness and abundance of radiating dendrites[66]. In fact, of the four cell types, this is the only case in which the dendritic tree-based classification performs better than the axonal tree-based classification (0.83 compared to 0.795). Interestingly, the dendritic tree-based classification performs poorly on chandelier cells (0.445), and with high rates of mis-classifications for bitufted and Martinotti cells. In contrast, the axonal tree-based classification, identified these cells as having a very high success rate (F_1-score of 0.928).

We next combined axonal and dendritic tree morphology parameters and applied the same classification scheme as before. This resulted in an improved classification performance: the average F_1-score changed from 0.837 for axonal trees and 0.619 for dendritic trees to 0.878 for the two combined (Fig. 2c). The corresponding sensitivity and precision values for all these classification schemes are presented in Supplementary Fig. S2.

The classification results for six interneuron types, also including the double-bouquet and basket cells, results in an average F_1-score of 0.752 for the axonal tree morphology, and an average F_1-score of 0.435 for the dendritic tree morphology (Supplementary Fig. S3). A remarkable similarity between the axonal trees of the double-bouquet and Martinotti cells is evident. This resemblance supports previous studies that showed the similarity between the electrophysiological properties of these two types of neurons[5,67]. A heatmap comparing the distributions of the morphological parameters for each interneuron type is presented in Supplementary Fig. S4.

The selected classification logistic regression models by axonal and dendritic trees store in them information about morphological features that are important for differentiating between interneuron types (Supplementary Fig. S5). For example, neurogliaform cells are characterized by symmetrical topology, high Sholl values at $100\mu m$, and high values of mean GR of the axonal tree. In the dendritic tree, however, they are characterized by low values of mean GR. In contrast, bitufted cells have low values of the mean GR in the axonal tree, and high values of mean GR in the dendritic tree. Chandelier cells have high values of mean branch length and mean branch length divided by the square root of diameter; Martinotti cells are characterized by high values of the maximum dendritic branch length and the maximum path length.

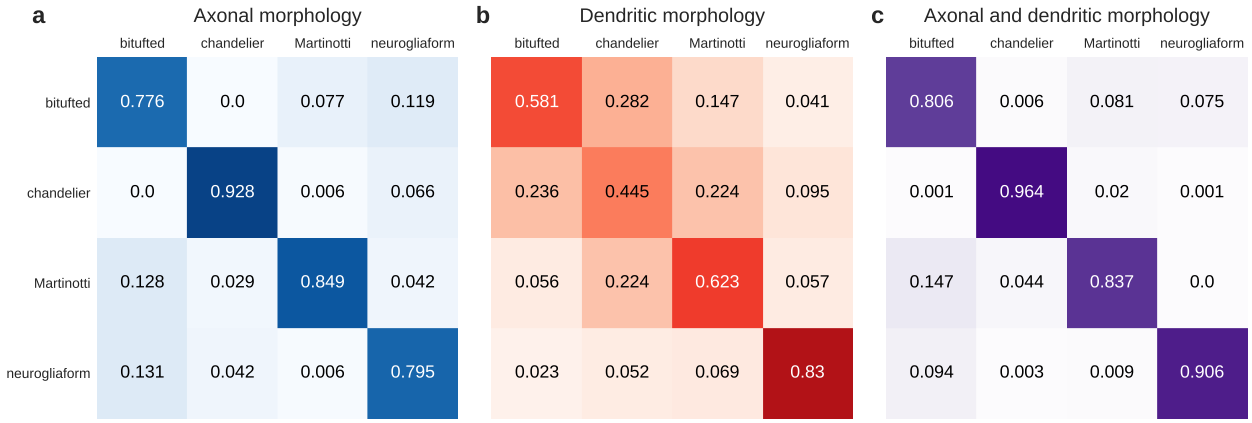

Figure 2: Classification by morphology. F_1-score matrices for **a.** Axonal tree morphology only (average F_1-score: 0.837), **b.** Dendritic tree morphology only (average F_1-score: 0.619), and **c.** Axonal and dendritic tree morphologies combined (average F_1-score: 0.878).

Classification of interneuron types by signal propagation dynamics

To study the signal propagation dynamics, we measured the response to current stimulus pulses injected into the soma at various frequencies along the axonal tree. Figure 3 presents an example of simulated neuronal activity along axonal branches of a basket cell. Figure 3a shows the experimental setup: the morphology of the neuron, depicted according to the digitally reconstructed morphology, the location in which the stimulus is induced, and the locations in which the propagated dynamics is recorded. In this example, we used the membrane properties of the 'continuous non-accommodating' (cNAC) e-type, obtained from the BBP repertoire to simulate signal propagation. Figure 3b shows electrical activity patterns observed in four points along the axonal tree. In the soma, all the stimulus pulses lead to action potential (denoted as '0'), and in the other probed locations intermitted trains occurred (denoted as '1-3'). Figure 3c presents an 'axonogram' of the axonal tree of the neuron presented in Fig. 3a. Each axonal branch appears as a separate line, with the line width proportional to the branch diameter. Figure 3d is a raster plot of the spikes' timing along each branch of the axonal tree. The branch color in the axonogram (Fig. 3c) corresponds to the firing pattern measured along it.

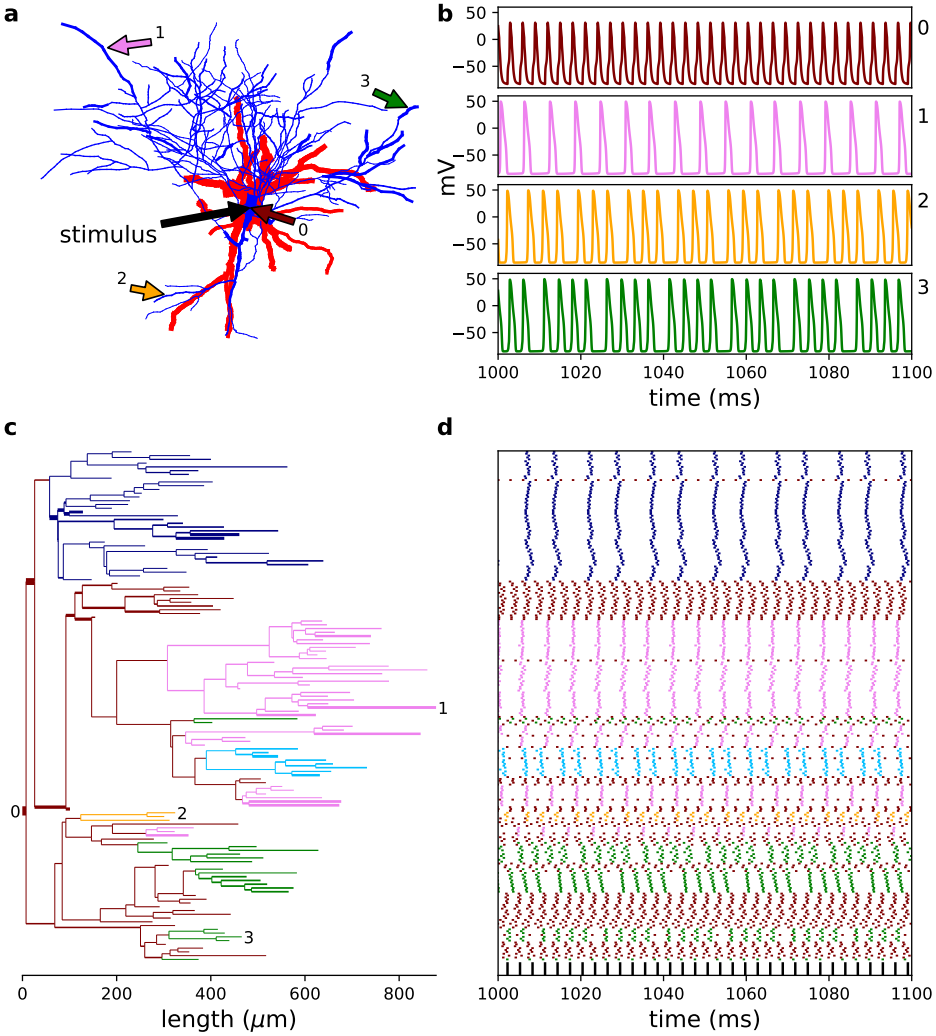

Figure 3: Activity recorded along the axonal tree. a. An XY projection for the NMO_06143 interneuron[27]. Axons are in blue and dendrites are in red. **b.** An example of firing patterns in four different locations. Panels 0-3 (indicated in the top right part of each graph) correspond to the arrows shown in **a**. **c.** Axonogram: a dendrogram of the axonal tree only. Horizontal line widths indicate axonal diameters. Line color indicates the fraction of spike train that propagates: maroon - 1, orange - 0.75, deep sky blue - 0.66, violet - 0.5, and navy - 0.375. **d.** Raster plot of the electrical activity; each row represents the activity at the corresponding (same height) axonal branch in **c**. Black squares on the bottom row indicate the current pulses applied to the soma ($330Hz$). The response to the first $1,000ms$ is not shown, to rule out the influence of the initial condition.

Figure 4 shows the electrical response along the axonal tree for different stimulus frequencies for the cNAC e-type. At $200Hz$ (Fig. 4a) the axonal tree is split into two subtrees, each exhibiting a different firing pattern, in particular, an uninterrupted train and a '1:1' pattern in which only every other pulse propagates. For a stimulus frequency of $300Hz$ (Fig. 4b), there are 8 subtrees with three different response types, and at $400Hz$ (Fig. 4c), there are 23 subtrees with five different response types. Figure 4d presents the number of subtrees as a function of stimulus frequency (blue curve). The dots (marked in 'a', 'b', and 'c') correspond to the scenarios presented in Figs 4a, 4b, and 4c. In addition to cNAC, three other e-types were considered for propagating dynamics: cAC, bAC, and bNAC. The decision to focus on these e-types resulted from an analysis that showed a high degree of propagating signal similarity between e-types (see Supplementary Fig. S6). The number of subtrees, generated for the cAC, bNAC, and bAC e-types, are presented in Fig. 4d (dashed curves, and see Supplementary Figs S7-S9).

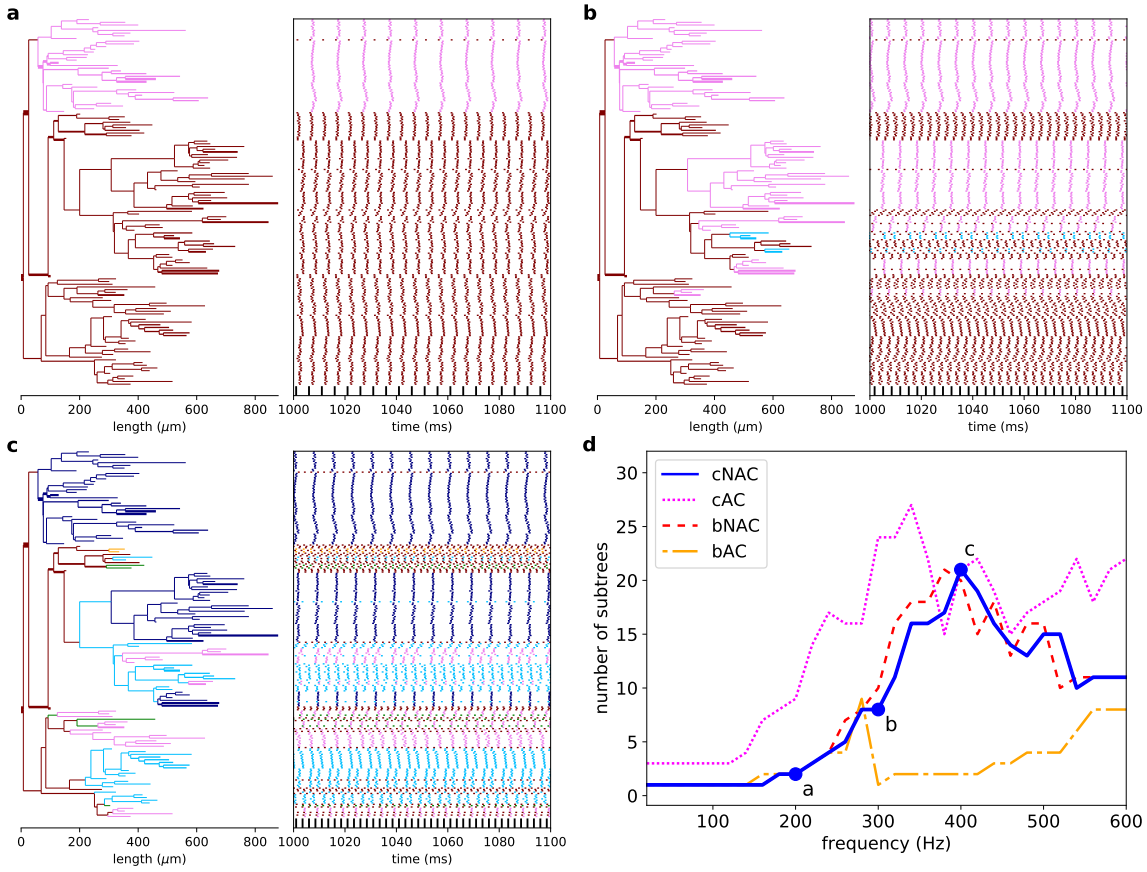

Figure 4: Effects of stimulus frequency on the signal propagation dynamics. Axonograms showing the responses of the same interneuron (as in Fig. 3) to three stimulus frequencies are presented in **a.** $(200Hz)$, **b.** $(300Hz)$, and **c.** $(400Hz)$. The number of subtrees as a function of stimulus frequency is plotted in **d.**

We then tested the possibility of using neuronal activity signatures to classify interneuron types. To this end, we have engineered activity-based features from Hill diversity indexes[68] (see Methods). Figure 5 shows the mean and standard deviation of the $q = 0$ diversity index as a function of the stimulus frequency. Note that when $q = 0$, the diversity index is equal to the number of subtrees. Detailed graphs for three Hill diversity indexes ($q = 0$, $q = 1$, and $q = 100$) for the six interneuron types are presented in Supplementary Fig. S10. Neurons were classified using multinomial logistic regression, and assessed with a 16-fold cross validation scheme with 1,000 repeats. Figure 6 presents the classification results in terms of F_1-score for three scenarios: axonal tree morphology (Fig. 6a), axonal tree activity (Fig. 6b), and a combination of both (Fig. 6c). The corresponding sensitivity and precision values of these classification schemes are presented in Supplementary Fig. S11. Combining the axonal morphology with axonal tree activity improves the classification's average F_1-score from 0.837 to 0.843. The classification results for the six interneuron types are presented in Supplementary Fig. S12.

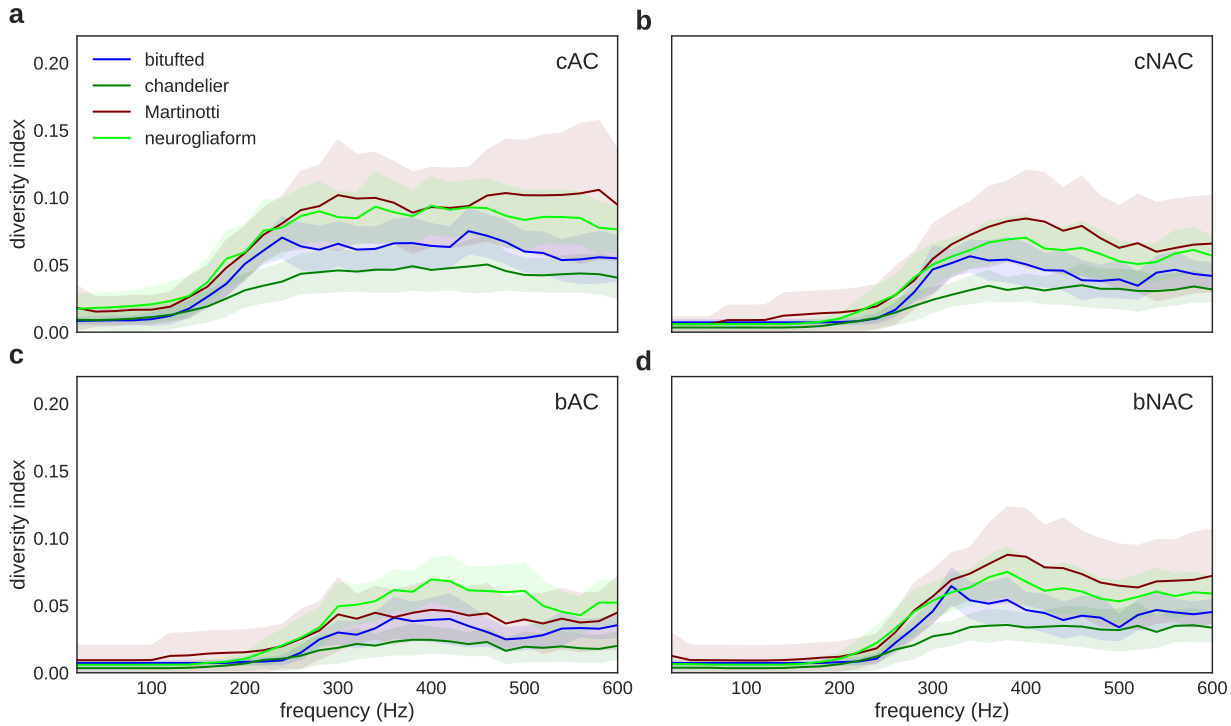

Figure 5: Axonal response characterized by diversity index as a function of stimulus frequency. Solid lines represent the mean diversity index ($q = 0$) normalized by the number of branches, and the shaded regions represent plus minus one standard deviation. Each panel shows the response for another e-type: **a.** Continuous accommodating (cAC), **b.** Continuous non-accommodating (cNAC), **c.** Burst accommodating (bAC), and **d.** Burst non-accommodating (bNAC).

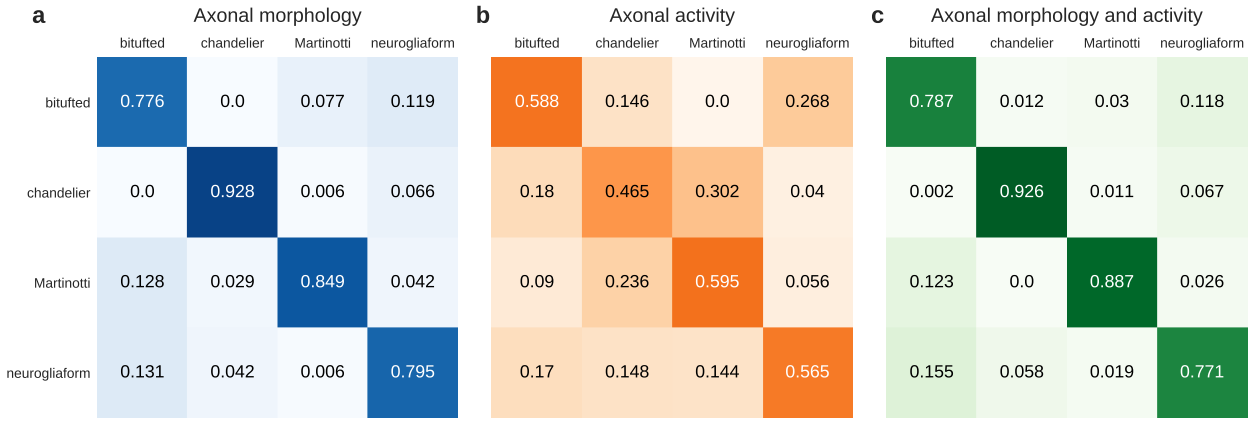

Figure 6: Classification by activity. F_1-score matrices for **a.** Axonal tree morphology only (average F_1-score: 0.837, same as Fig. 2a), **b.** Activity only (average F_1-score: 0.553), and **c.** Axonal morphology and activity combined (average F_1-score: 0.843).

Discrimination between pyramidal cells and interneurons

We extended the study to include excitatory neurons as well, and classified neurons into two classes: interneurons and pyramidal cells. All pyramidal and interneuron reconstructions were downloaded from the *NeuroMorpho.Org* database, and filtered for several criteria to obtain a high-quality dataset for classification (Table 2). Reconstructions with fewer than 20 axonal branches, fewer than 1,000 axonal segments, and fewer than 20 different axonal diameter values measured were discarded. The resulting filtered dataset is diverse because the neurons were taken from different brain regions of male and female rats (n=225, 66%), mice (n=77, 23%), and humans (n=36, 11%), and were analyzed by different labs.

Filter criteria	Pyramidal cells	Interneurons
All data in NeuroMorpho.Org 7.4	22,428	19,419
Neurons with axon data	3,102	8,071
≥ 20 axonal branches and $\geq 1,000$ axonal segments	1,034	1,439
≥ 20 axonal diameter values measured	146	192

Table 2: Pyramidal and interneuron reconstruction filtration. The table summarizes the number of pyramidal cells and interneurons that were included after each filtration step.

For this classification we used the same 28 morphological parameters used for the interneuron classification (Supplementary Table S1). To avoid biases due to unequal group sizes, we down-sampled the interneurons to include 146 randomly selected cells. The distribution of these morphological parameters for the pyramidal cells and interneurons are presented in Supplementary Fig. S13. Logistic regression was used for classification, and a 4-fold cross validation scheme with 1,000 repeats was applied. The F_1-score classification results are presented in Fig. 7a, demonstrating a very good classification with an average F_1-score of 0.921. The corresponding sensitivity and precision are presented in Supplementary Fig. S14. Supplementary Fig. S15 shows the logistic regression's coefficients, indicating the significance of each morphological feature in discriminating between pyramidal cells and interneurons. The most significant parameters are the number of branches, a Sholl radius of $300\mu m$, the mean branch diameter, and the number of GR values larger than three. Here as well, signal propagation dynamics was simulated using the 'cAD' e-type, and a diversity index was calculated. The mean and standard deviation of this diversity index for the 146 pyramidal cells is presented in Fig. 7b. One can see that the diversity index begins to increase at lower frequencies (around $100Hz$), compared with those of the four e-types of interneurons (Fig. 5). Since pyramidal cells have different e-types compared with interneurons, activity-based classification was not pursued here.

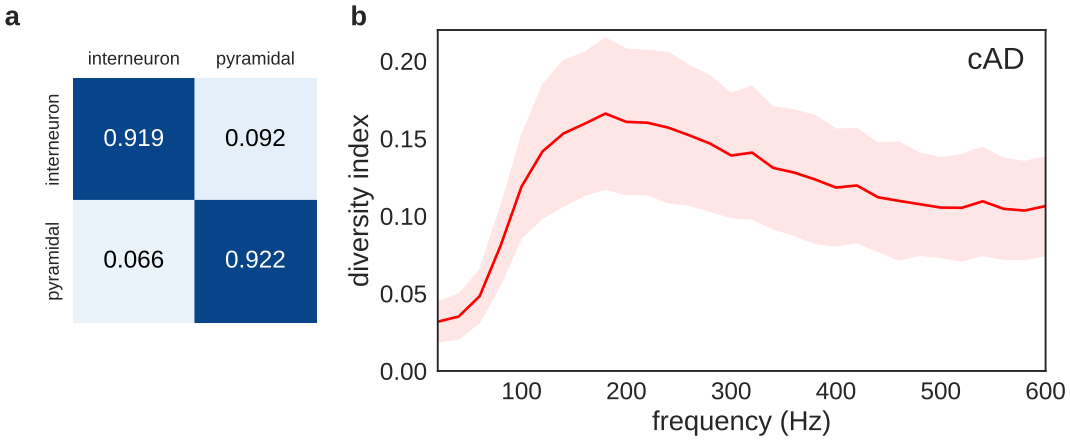

Figure 7: Classification of interneurons and pyramidal cells. a. F_1-score matrix. **b.** Axonal response characterized by the diversity index as a function of stimulus frequency for 146 pyramidal cells, using the continuous adapting (cAD) e-type. Solid lines represent the mean diversity index ($q = 0$) normalized by the number of branches, and the shaded regions represent plus minus one standard deviation.

An interesting question in terms of signal propagation dynamics is whether the response at a branching point is symmetric between the two sibling branches[69,70]. To address this question, we characterized the type of response in interneurons and pyramidal cells, as a function of stimulus frequency, for the cAC, cNAC, bAC, bNAC, and cAD e-types. The simulation results of the 192 interneurons and the 146 pyramidal cells reveal a mixture of symmetric and asymmetric responses. The ratio between the number of symmetric and asymmetric responses approached one in interneurons for all e-types and frequencies tested. In pyramidal cells we observed more symmetric responses than asymmetric responses (Supplementary Fig. S16).

Discussion

Numerous studies published in recent years used a variety of approaches to classify cortical interneurons. These studies raised many questions regarding the identification of neuronal types and whether interneurons can be described by either a set of distinct classes or by a continuum of phenotypes[26]. Standard classifications approaches are based on morphology. In particular, they utilize soma position, dendritic geometry, axonal projections, and connectivity features. Here we used *axonal tree morphology* for interneuron classification, resulting in better classification compared with classification based on the dendritic tree morphology. Combining axonal tree morphology with dendritic tree morphology and activity patterns further improved the classification results. For the data analyzed here, the average F_1-score changed from 0.837 for axonal trees and 0.619 for dendritic trees to 0.878 for the two combined. It remains open to study whether additional properties, such as electrophysiology, molecularity, and transcriptomics will further improve the classification.

Interneuron subtypes are known to shape the electrophysiological activity dynamics[71,72], and therefore, the use of functionally relevant parameters as classifiers is important[73–75]. In this study, an emphasis was given to morphological parameters related to modulation of firing patterns. To this end, we recorded simulated activity along each branch of the axonal tree, and not only at the soma. This revealed diverse response patterns already at the single cell level. Importantly, we showed that these firing patterns can be used to classify interneurons into their known subtypes. Axonal tree responses were recorded in a wide range of spike train frequencies (up to $600Hz$), since it was recently shown that high-frequency trains may exist in fast-spiking neurons and in the rapid spikes of bursting[76,77].

Previous studies have shown how dendritic tree geometry affects the electrical activity in neurons[78–81]. It was demonstrated that in activity simulations taking into account the dendritic tree morphology, rather than a point neuron, can capture local non-linear effects[82,83]. Our results indicate that it is beneficial to include the full biophysical neuronal structure, including the axonal tree, for modeling neuronal activity propagation. In particular, precise measurements of neuronal processes were shown here to strongly affect simulation results in single cell models.

Despite tremendous progress in imaging and reconstruction techniques, there is still excessive inter-laboratory variability[8]. Rigorous data standards are lacking and can greatly improve future studies. More data of high-resolution reconstructions from diverse sources are of utmost importance for more comprehensive species dependent neuron classification. When such additional data become available, neurons of rats, mice, and humans, from different brain regions and layers, could be independently classified. The electrical membrane properties of the reconstructions used here, were fitted by the BBP only to the axon initial segment, and do not include axonal boutons and myelin sheath effects along the axonal tree[52]. Nevertheless, these properties resemble a close approximation of an actual mechanism, and yielded very good classifications. Fitting the electrical membrane properties along all the axonal tree, can further improve our understanding of signal propagation in neurons.

The classification schemes introduced here can be utilized to robustly define neuronal subtypes in a functionally relevant manner. Axonal tree morphology and activity can be utilized as well in an unsupervised fashion to define subtypes. This can advance standardization toward consensus regarding neuronal type nomenclature.

Methods

Simulations

Digitally reconstructed neurons were downloaded from *NeuroMorpho.Org* version 7.4 (released: 4/16/2018)[55]. Each neuron's reconstructed data is stored in an SWC file. We used the notation of branch to describe an axonal section between two branching points, or between a branching point and a termination point (leaf), and a segment to describe a small compartment in 3D space. Several successive segments were used to construct a branch (in line with[84]). The SWC files were imported into *NEURON* simulation using the *Import3D* tool, which converts all the segments of each branch into equivalent diameter cables. The neuronal activity simulations were conducted using *NEURON* simulation environment version 7.5 embedded in Python 2.7.13[85,86]. The same version of Python was used for all other analyses presented here.

Membrane electrical properties

To simulate signal propagation dynamics, ion channel mechanisms with different densities were introduced into the reconstructed neurons. For realistic modeling, we used membrane properties borrowed from the BBP[51,52]. These e-types were fitted to experiments produced in the cortex neurons of Wistar (Han) rats at a temperature of $34^{\circ}C$. Each e-type is constructed from specific ion channel types with varying densities at the soma, axons, and basal and apical dendrites. Details of the ion channels, their kinetics, and other parameters can be found in the NMC portal[51] and in the attached files there. The specific equations and parameters used here were taken from the following reconstructions: L23_LBC_cNAC187_5, L23_DBC_cACint209_1, L23_LBC_bNAC219_1, L5_LBC_bAC217_4, and L5_STPC_cADpyr.

Current pulses were stimulated in the soma, with an amplitude of $20\mu A$ and a duration of $1ms$, for a range of frequencies. Electrical responses were recorded at the center of each axonal branch. For the raster plots (e.g., Fig. 3d), a spike was defined when the voltage peak amplitude exceeded a zero voltage threshold. Voltage peaks that were separated by less than $1ms$ were discarded to avoid discretization errors.

Classification

Supervised classification was performed using multinomial logistic regression. We used the *LogisticRegression* function from the *Scikit-learn* python library, with an L^2 regularization penalty. For the classification based on morphological parameters, 1,000 4-fold cross validation repeats were produced, i.e., 1,000 choices of 75% of the data for training and 25% for testing the model. All morphological parameters were first log-transformed, and then standardized for this classification. The parameters for both the training and test sets were standardized according to the mean and standard deviation of the training set. To select more relevant features (feature selection), the top 15 features of the initial logistic regression model were used for the final model. Sensitivity was calculated by normalizing each value in the confusion matrix by the sum of the row to which it belongs. Precision was calculated similarly but normalization was done according to the column of the confusion matrix. F_1-score is defined as the harmonic average of sensitivity and precision (Equation 1).

$$F_1 = 2 \times \frac{precision \times sensitivity}{precision + sensitivity} \tag{1}$$

For activity-based classification, the mean and the standard deviation of the Hill diversity index (Equation 2) were calculated as a function of frequency for each interneuron type in the training set. The Hill diversity index[68] was calculated for $q \in \{0, 1, 100\}$, for four e-types, and two definitions of a subgroup: 1. A subtree with an identical response, and 2. A set of branches with an identical response (possibly in more than one subtree). The Hill diversity index is defined as

$${}^{q}D = \left(\sum_{i=1}^{R} P_i^q \right)^{1/(1-q)} \tag{2}$$

where R is the number of groups ("species" according to its original definition), and P_i is the normalized number of members in each group. ${}^{0}D$ equals the number of groups. ${}^{1}D$ converges to the

exponent of Shanon Entropy (Equation 3), and ${}^{\infty}D$ approaches one over the fraction of the largest group.

$$ {}^{1}D = exp\Big(-\sum_{i=1}^{R} P_i ln(p_i) \Big) \tag{3} $$

For each neuron from the test set, the Hill diversity index was calculated, following by calculating the distance to the mean index of each interneuron type in the training set in units of standard deviation (Equation 4). To avoid singularities, $\epsilon = 0.01$ was added quadratically to the variance:

$$ \sqrt{\sum_{i} \frac{|\bar{D}_i - D_i|^2}{\sigma_i^2 + \epsilon^2}} \tag{4} $$

Each diversity curve (e.g., Fig. 5) was normalized by the number of axonal branches.

Code availability

The code for the models and simulations will be publicly available on Github upon publication.

References

[1] Seung HS, Sümbül U. Neuronal cell types and connectivity: lessons from the retina. Neuron. 2014;83(6):1262–1272.

[2] Harris KD, Shepherd GM. The neocortical circuit: themes and variations. Nature neuroscience. 2015;18(2):170.

[3] Tremblay R, Lee S, Rudy B. GABAergic interneurons in the neocortex: from cellular properties to circuits. Neuron. 2016;91(2):260–292.

[4] Hamilton DJ, Wheeler D, White C, Rees C, Komendantov AO, Bergamino M, et al. Name-calling in the hippocampus (and beyond): coming to terms with neuron types and properties. Brain informatics. 2017;4(1):1–12.

[5] Burkhalter A. Many specialists for suppressing cortical excitation. Frontiers in neuroscience. 2008;2(2):155.

[6] Costa LDF, Zawadzki K, Miazaki M, Viana MP, Taraskin S. Unveiling the neuromorphological space. Frontiers in computational neuroscience. 2010;4:150.

[7] Santana R, McGarry LM, Bielza C, Larrañaga P, Yuste R. Classification of neocortical interneurons using affinity propagation. Frontiers in neural circuits. 2013;7.

[8] Polavaram S, Gillette TA, Parekh R, Ascoli GA. Statistical analysis and data mining of digital reconstructions of dendritic morphologies. Frontiers in neuroanatomy. 2014;8.

[9] Armañanzas R, Ascoli GA. Towards the automatic classification of neurons. Trends in neurosciences. 2015;38(5):307–318.

[10] Vasques X, Vanel L, Villette G, Cif L. Morphological Neuron Classification Using Machine Learning. Frontiers in neuroanatomy. 2016;10.

[11] Zeng H, Sanes JR. Neuronal cell-type classification: challenges, opportunities and the path forward. Nature Reviews Neuroscience. 2017;18(9):530.

[12] DeFelipe J, López-Cruz PL, Benavides-Piccione R, Bielza C, Larrañaga P, Anderson S, et al. New insights into the classification and nomenclature of cortical GABAergic interneurons. Nature Reviews Neuroscience. 2013;14(3):202.

[13] Druckmann S, Hill S, Schürmann F, Markram H, Segev I. A hierarchical structure of cortical interneuron electrical diversity revealed by automated statistical analysis. Cerebral Cortex. 2012;23(12):2994–3006.

[14] Ferrante M, Tahvildari B, Duque A, Hadzipasic M, Salkoff D, Zagha EW, et al. Distinct functional groups emerge from the intrinsic properties of molecularly identified entorhinal interneurons and principal cells. Cerebral Cortex. 2016;27(6):3186–3207.

[15] Komendantov AO, Venkadesh S, Rees CL, Wheeler DW, Hamilton DJ, Ascoli GA. Firing pattern classification and phenotyping in a knowledge base of hippocampal neuron types. bioRxiv. 2017; p. 212084.

[16] Rudy B, Fishell G, Lee S, Hjerling-Leffler J. Three groups of interneurons account for nearly 100% of neocortical GABAergic neurons. Developmental neurobiology. 2011;71(1):45–61.

[17] Kepecs A, Fishell G. Interneuron cell types are fit to function. Nature. 2014;505(7483):318–326.

[18] Jiang X, Shen S, Cadwell CR, Berens P, Sinz F, Ecker AS, et al. Principles of connectivity among morphologically defined cell types in adult neocortex. Science. 2015;350(6264):aac9462.

[19] Bloss EB, Cembrowski MS, Karsh B, Colonell J, Fetter RD, Spruston N. Structured dendritic inhibition supports branch-selective integration in CA1 pyramidal cells. Neuron. 2016;89(5):1016–1030.

[20] Huang ZJ. Toward a genetic dissection of cortical circuits in the mouse. Neuron. 2014;83(6):1284–1302.

[21] Zeisel A, Muñoz-Manchado AB, Codeluppi S, Lönnerberg P, La Manno G, Juréus A, et al. Cell types in the mouse cortex and hippocampus revealed by single-cell RNA-seq. Science. 2015;347(6226):1138–1142.

[22] Tasic B, Menon V, Nguyen TN, Kim TK, Jarsky T, Yao Z, et al. Adult mouse cortical cell taxonomy revealed by single cell transcriptomics. Nature neuroscience. 2016;19(2):335–346.

[23] Luo C, Keown CL, Kurihara L, Zhou J, He Y, Li J, et al. Single-cell methylomes identify neuronal subtypes and regulatory elements in mammalian cortex. Science. 2017;357(6351):600–604.

[24] Lein E, Borm LE, Linnarsson S. The promise of spatial transcriptomics for neuroscience in the era of molecular cell typing. Science. 2017;358(6359):64–69.

[25] Chevée M, Robertson JDJ, Cannon GH, Brown SP, Goff LA. Variation in Activity State, Axonal Projection, and Position Define the Transcriptional Identity of Individual Neocortical Projection Neurons. Cell Reports. 2018;22(2):441–455.

[26] Dumitriu D, Cossart R, Huang J, Yuste R. Correlation between axonal morphologies and synaptic input kinetics of interneurons from mouse visual cortex. Cerebral cortex. 2006;17(1):81–91.

[27] Karagiannis A, Gallopin T, Dávid C, Battaglia D, Geoffroy H, Rossier J, et al. Classification of NPY-expressing neocortical interneurons. Journal of Neuroscience. 2009;29(11):3642–3659.

[28] McGarry LM, Packer AM, Fino E, Nikolenko V, Sippy T, Yuste R. Quantitative classification of somatostatin-positive neocortical interneurons identifies three interneuron subtypes. Frontiers in neural circuits. 2010;4.

[29] Hosp JA, Strüber M, Yanagawa Y, Obata K, Vida I, Jonas P, et al. Morpho-physiological criteria divide dentate gyrus interneurons into classes. Hippocampus. 2014;24(2):189–203.

[30] Sümbül U, Song S, McCulloch K, Becker M, Lin B, Sanes JR, et al. A genetic and computational approach to structurally classify neuronal types. Nature communications. 2014;5:3512.

[31] Staiger JF, Loucif AJ, Schubert D, Möck M. Morphological characteristics of electrophysiologically characterized layer Vb pyramidal cells in rat barrel cortex. PloS one. 2016;11(10):e0164004.

[32] Helmstaedter M, Sakmann B, Feldmeyer D. The relation between dendritic geometry, electrical excitability, and axonal projections of L2/3 interneurons in rat barrel cortex. Cerebral Cortex. 2008;19(4):938–950.

[33] Helmstaedter M, Sakmann B, Feldmeyer D. L2/3 interneuron groups defined by multiparameter analysis of axonal projection, dendritic geometry, and electrical excitability. Cerebral Cortex. 2008;19(4):951–962.

[34] Cervantes EP, Comin CH, Cesar RM, da Fontoura Costa L. Data-oriented neuron classification from their parts. In: e-Science (e-Science), 2016 IEEE 12th International Conference on. IEEE; 2016. p. 243–250.

[35] Papoutsi A, Kastellakis G, Poirazi P. Basal tree complexity shapes functional pathways in the prefrontal cortex. Journal of Neurophysiology. 2017;118(4):1970–1983.

[36] Mihaljević B, Bielza C, Benavides-Piccione R, DeFelipe J, Larrañaga P. Multi-dimensional classification of GABAergic interneurons with Bayesian network-modeled label uncertainty. Frontiers in computational neuroscience. 2014;8.

[37] Mihaljević B, Benavides-Piccione R, Guerra L, DeFelipe J, Larrañaga P, Bielza C. Classifying GABAergic interneurons with semi-supervised projected model-based clustering. Artificial intelligence in medicine. 2015;65(1):49–59.

[38] Wheeler DW, White CM, Rees CL, Komendantov AO, Hamilton DJ, Ascoli GA. Hippocampome. org: a knowledge base of neuron types in the rodent hippocampus. Elife. 2015;4.

[39] Kanari L, Dłotko P, Scolamiero M, Levi R, Shillcock J, Hess K, et al. A topological representation of branching neuronal morphologies. Neuroinformatics. 2017; p. 1–11.

[40] Li Y, Wang D, Ascoli GA, Mitra P, Wang Y. Metrics for comparing neuronal tree shapes based on persistent homology. PloS one. 2017;12(8):e0182184.

[41] Hernández-Pérez LA, Delgado-Castillo D, Martín-Pérez R, Orozco-Morales R, Lorenzo-Ginori JV. New Features for Neuron Classification. Neuroinformatics. 2018; p. 1–21.

[42] Kanari L, Ramaswamy S, Shi Y, Morand S, Meystre J, Perin R, et al. Objective Classification of Neocortical Pyramidal Cells. bioRxiv. 2018; p. 349977.

[43] Gillette TA, Ascoli GA. Topological characterization of neuronal arbor morphology via sequence representation: I-motif analysis. BMC bioinformatics. 2015;16(1):216.

[44] Gillette TA, Hosseini P, Ascoli GA. Topological characterization of neuronal arbor morphology via sequence representation: II-global alignment. BMC bioinformatics. 2015;16(1):209.

[45] Wan Y, Long F, Qu L, Xiao H, Hawrylycz M, Myers EW, et al. BlastNeuron for automated comparison, retrieval and clustering of 3D neuron morphologies. Neuroinformatics. 2015;13(4):487–499.

[46] Li T, Tian C, Scalmani P, Frassoni C, Mantegazza M, Wang Y, et al. Action potential initiation in neocortical inhibitory interneurons. PLoS biology. 2014;12(9):e1001944.

[47] Casale AE, Foust AJ, Bal T, McCormick DA. Cortical interneuron subtypes vary in their axonal action potential properties. Journal of Neuroscience. 2015;35(47):15555–15567.

[48] Druckmann S, Banitt Y, Gidon AA, Schürmann F, Markram H, Segev I. A novel multiple objective optimization framework for constraining conductance-based neuron models by experimental data. Frontiers in neuroscience. 2007;1:1.

[49] Van Geit W, Gevaert M, Chindemi G, Rössert C, Courcol JD, Muller EB, et al. BluePyOpt: leveraging open source software and cloud infrastructure to optimise model parameters in neuroscience. Frontiers in neuroinformatics. 2016;10:17.

[50] Ascoli GA, Alonso-Nanclares L, Anderson SA, Barrionuevo G, Benavides-Piccione R, Burkhalter A, et al. Petilla terminology: nomenclature of features of GABAergic interneurons of the cerebral cortex. Nature Reviews Neuroscience. 2008;9(7):557–568.

[51] Ramaswamy S, Courcol JD, Abdellah M, Adaszewski SR, Antille N, Arsever S, et al. The neocortical microcircuit collaboration portal: a resource for rat somatosensory cortex. Frontiers in neural circuits. 2015;9.

[52] Markram H, Muller E, Ramaswamy S, Reimann MW, Abdellah M, Sanchez CA, et al. Reconstruction and simulation of neocortical microcircuitry. Cell. 2015;163(2):456–492.

[53] Gouwens NW, Berg J, Feng D, Sorensen SA, Zeng H, Hawrylycz MJ, et al. Systematic generation of biophysically detailed models for diverse cortical neuron types. Nature communications. 2018;9(1):710.

[54] Gouwens NW, Sorensen SA, Berg J, Lee C, Jarsky T, Ting J, et al. Classification of electrophysiological and morphological types in mouse visual cortex. bioRxiv. 2018;doi:10.1101/368456.

[55] Ascoli GA, Donohue DE, Halavi M. NeuroMorpho.Org: a central resource for neuronal morphologies. Journal of Neuroscience. 2007;27(35):9247–9251.

[56] Markram H, Toledo-Rodriguez M, Wang Y, Gupta A, Silberberg G, Wu C. Interneurons of the neocortical inhibitory system. Nature Reviews Neuroscience. 2004;5(10):793–807.

[57] Feldmeyer D, Qi G, Emmenegger V, Staiger JF. Inhibitory interneurons and their circuit motifs in the many layers of the barrel cortex. Neuroscience. 2018;368:132–151.

[58] Toledo-Rodriguez M, Goodman P, Illic M, Wu C, Markram H. Neuropeptide and calcium-binding protein gene expression profiles predict neuronal anatomical type in the juvenile rat. The Journal of physiology. 2005;567(2):401–413.

[59] Scorcioni R, Polavaram S, Ascoli GA. L-Measure: a web-accessible tool for the analysis, comparison and search of digital reconstructions of neuronal morphologies. Nature protocols. 2008;3(5):866–876.

[60] Bozelos P, Stefanou SS, Bouloukakis G, Melachrinos C, Poirazi P. REMOD: A Tool for Analyzing and Remodeling the Dendritic Architecture of Neural Cells. Frontiers in neuroanatomy. 2016;9:156.

[61] Sholl DA. Dendritic organization in the neurons of the visual and motor cortices of the cat. Journal of anatomy. 1953;87(Pt 4):387.

[62] Ofer N, Shefi O, Yaari G. Branching morphology determines signal propagation dynamics in neurons. Scientific Reports. 2017;7.

[63] Goldstein SS, Rall W. Changes of action potential shape and velocity for changing core conductor geometry. Biophysical journal. 1974;14(10):731–757.

[64] ODonnell C, van Rossum MC. Spontaneous action potentials and neural coding in unmyelinated axons. Neural computation. 2015;.

[65] Ofer N, Shefi O. Axonal geometry as a tool for modulating firing patterns. Applied Mathematical Modelling. 2016;40(4):3175–3184.

[66] Overstreet-Wadiche L, McBain CJ. Neurogliaform cells in cortical circuits. Nature Reviews Neuroscience. 2015;16(8):458.

[67] Krimer LS, Zaitsev AV, Czanner G, Kroner S, González-Burgos G, Povysheva NV, et al. Cluster analysis–based physiological classification and morphological properties of inhibitory neurons in layers 2–3 of monkey dorsolateral prefrontal cortex. Journal of neurophysiology. 2005;94(5):3009–3022.

[68] Hill MO. Diversity and evenness: a unifying notation and its consequences. Ecology. 1973;54(2):427–432.

[69] Grossman Y, Parnas I, Spira M. Differential conduction block in branches of a bifurcating axon. The Journal of physiology. 1979;295(1):283–305.

[70] Parnas I, Segev I. A mathematical model for conduction of action potentials along bifurcating axons. The Journal of physiology. 1979;295(1):323–343.

[71] Klausberger T, Somogyi P. Neuronal diversity and temporal dynamics: the unity of hippocampal circuit operations. Science. 2008;321(5885):53–57.

[72] Chen G, Zhang Y, Li X, Zhao X, Ye Q, Lin Y, et al. Distinct Inhibitory Circuits Orchestrate Cortical beta and gamma Band Oscillations. Neuron. 2017;96(6):1403–1418.

[73] Sharpee TO. Toward functional classification of neuronal types. Neuron. 2014;83(6):1329–1334.

[74] Hardcastle K, Ganguli S, Giocomo LM. Cell types for our sense of location: where we are and where we are going. Nature neuroscience. 2017;20(11):1474.

[75] Emmenegger V, Qi G, Wang H, Feldmeyer D. Morphological and Functional Characterization of Non-fast-Spiking GABAergic Interneurons in Layer 4 Microcircuitry of Rat Barrel Cortex. Cerebral Cortex. 2018;.

[76] Eyal G, Mansvelder HD, de Kock CP, Segev I. Dendrites impact the encoding capabilities of the axon. Journal of Neuroscience. 2014;34(24):8063–8071.

[77] Wang B, Ke W, Guang J, Chen G, Yin L, Deng S, et al. Firing Frequency Maxima of Fast-Spiking Neurons in Human, Monkey, and Mouse Neocortex. Frontiers in cellular neuroscience. 2016;10.

[78] Mainen ZF, Sejnowski TJ, et al. Influence of dendritic structure on firing pattern in model neocortical neurons. Nature. 1996;382(6589):363–366.

[79] Vetter P, Roth A, Häusser M. Propagation of action potentials in dendrites depends on dendritic morphology. Journal of neurophysiology. 2001;85(2):926–937.

[80] Van Ooyen A, Duijnhouwer J, Remme MW, van Pelt J. The effect of dendritic topology on firing patterns in model neurons. Network: Computation in neural systems. 2002;13(3):311–325.

[81] Yi GS, Wang J, Deng B, Wei XL. Morphology controls how hippocampal CA1 pyramidal neuron responds to uniform electric fields: a biophysical modeling study. Scientific Reports. 2017;7.

[82] Bono J, Wilmes KA, Clopath C. Modelling plasticity in dendrites: from single cells to networks. Current opinion in neurobiology. 2017;46:136–141.

[83] Jarvis S, Nikolic K, Schultz SR. Neuronal gain modulability is determined by dendritic morphology: A computational optogenetic study. PLoS computational biology. 2018;14(3):e1006027.

[84] Cuntz H, Forstner F, Borst A, Häusser M. The TREES toolboxprobing the basis of axonal and dendritic branching. Neuroinformatics. 2011;9(1):91–96.

[85] Carnevale NT, Hines ML. The NEURON book. Cambridge University Press; 2006.

[86] Hines ML, Davison AP, Muller E. NEURON and Python. Frontiers in neuroinformatics. 2009;3.

Axonal tree morphology and signal propagation dynamics improve neuronal classification

Netanel Ofer[1,2], Orit Shefi[1,2,*], and Gur Yaari[1,*]

[1]Faculty of Engineering, Bar Ilan University, Ramat Gan 5290002, Israel.
[2]Bar Ilan Institute of Nanotechnologies and Advanced Materials, Bar Ilan University, Ramat Gan 5290002, Israel.

Supplementary material

	Description
1	The number of branches
2	Symmetry - mean of the ratio between the number of children in each daughter branch
3	Maximum branch order
4	Mean branch order
5	Difference between maximum and minimum on the x-coordinates (μm)
6	Difference between maximum and minimum on the y-coordinates (μm)
7	Difference between maximum and minimum on the z-coordinates (μm)
8	Sholl analysis - the number of branch intersections at a radius of $100\mu m$ from the soma in 3D
9	Sholl analysis - the number of branch intersections at a radius of $200\mu m$ from the soma in 3D
10	Sholl analysis - the number of branch intersections at a radius of $300\mu m$ from the soma in 3D
11	The number of branches longer than $200\mu m$
12	The number of branches longer than $300\mu m$
13	The number of branches longer than $400\mu m$
14	Maximum path length, the distance from the soma to the farther leaf (μm)
15	Minimum path length, the distance from the soma to the closer leaf (μm)
16	Mean path length, the distance from the soma to the closer leaf (μm)
17	Maximum branch length (μm)
18	Mean branch length (μm)
19	The total length of all branches in the axonal tree (μm)
20	Maximum branch length divided by the square root of the branch diameter
21	Mean branch length divided by the square root of the branch diameter
22	Maximum branch diameter (μm)
23	Mean branch diameter (μm)
24	The number of GRs above 2
25	The number of GRs above 3
26	The maximum GR value of all branching points
27	The mean GR value of all branching points
28	The percentage the of bifurcations with GR above 2

Table S1: Morphological features of the axonal tree.

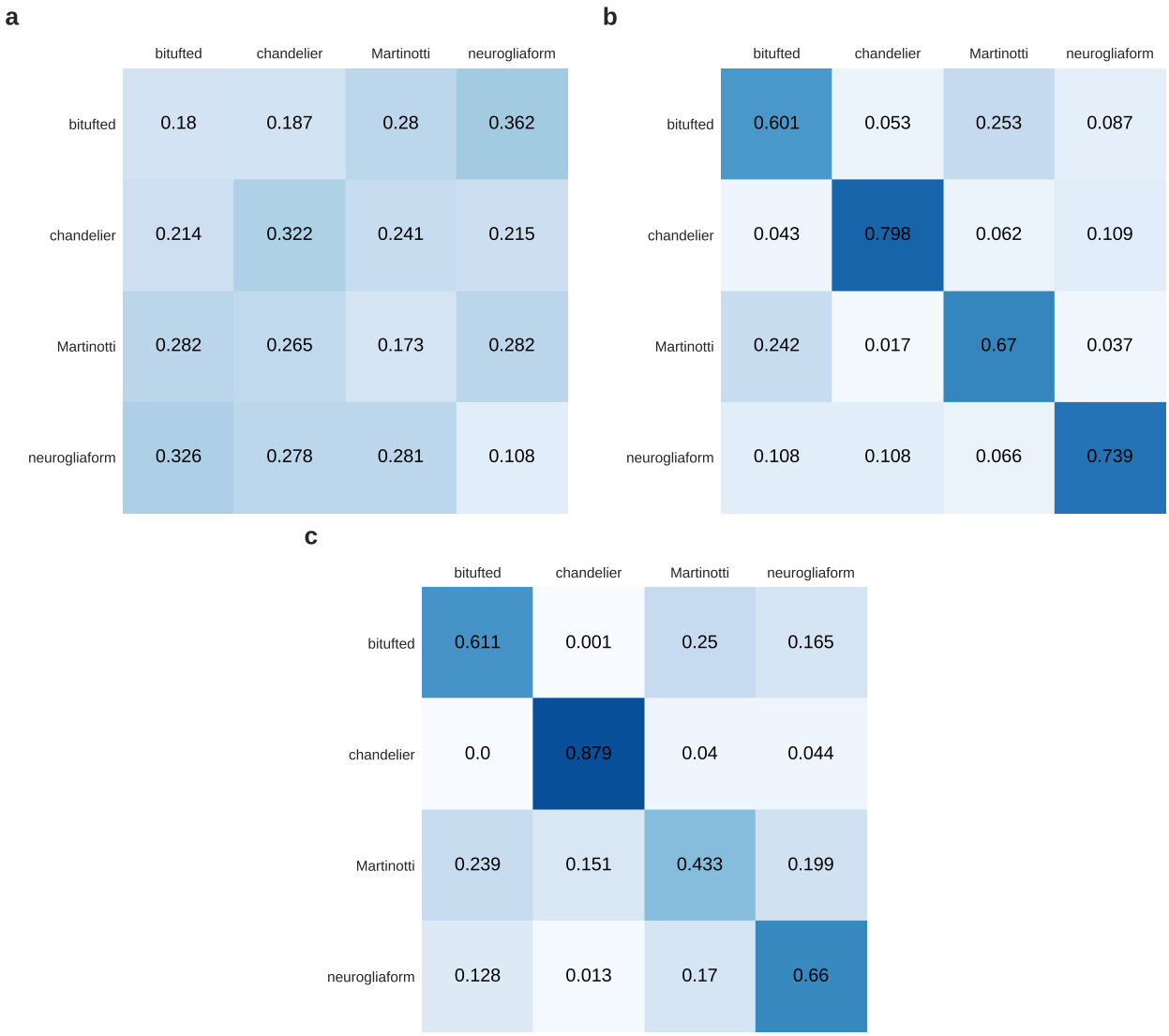

Figure S1: Validation classifications. a. Shuffled labels of the axonal tree morphology, average F_1-score: 0.196. **b.** 16 interneurons with the lowest number of diameter values measured in each cell type, with an average F_1-score: 0.702. **c.** 16 neurons with the highest resolution in each cell type were overwritten with radii of $1\mu m$. The resulting average F_1-score in this setup was 0.646.

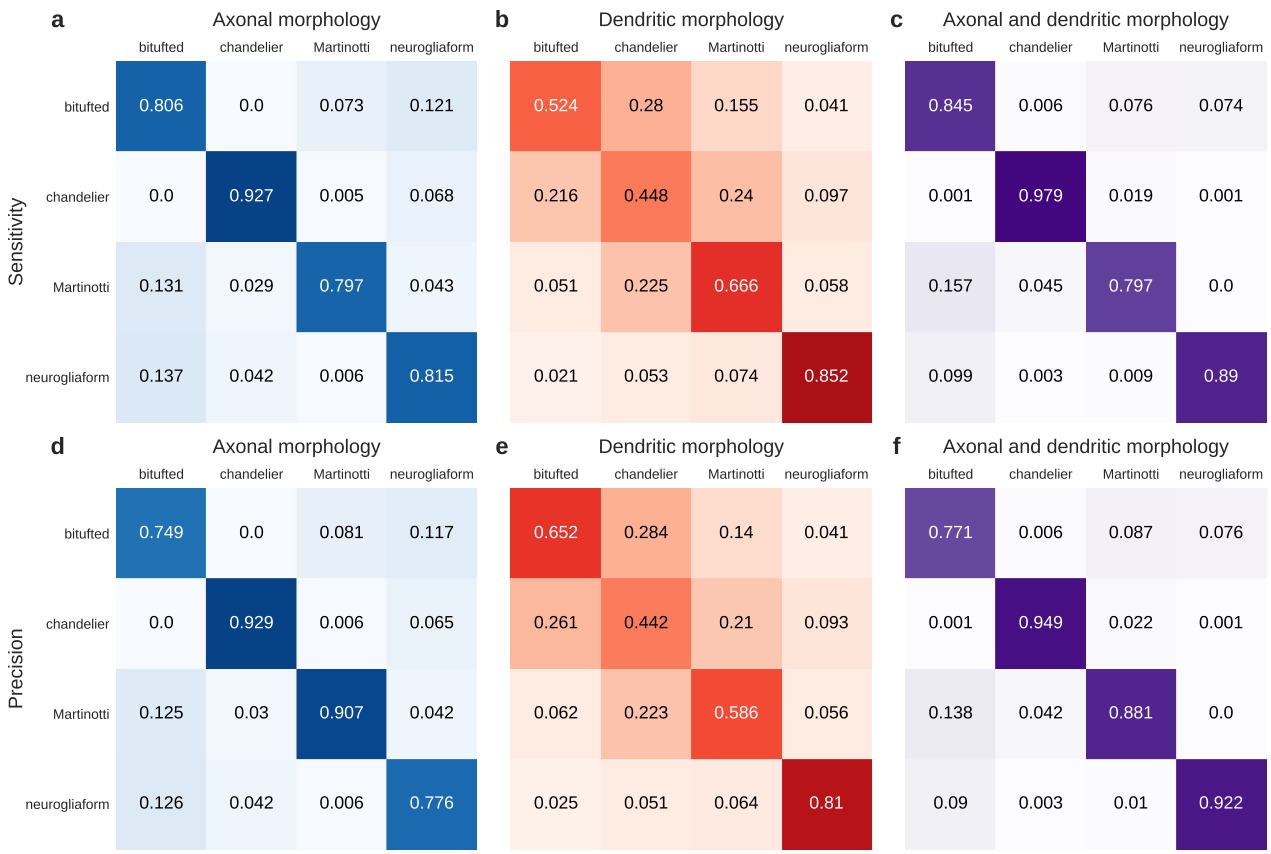

Figure S2: Classification by morphology - sensitivity and precision. Only axonal tree morphology, average sensitivity score: 0.836 (**a**), average precision score: 0.84 (**d**). Only dendritic tree morphology, average sensitivity score: 0.622 (**b**), average precision score: 0.622 (**e**). Axonal and dendritic tree morphology, average sensitivity score: 0.878 (**c**), average precision score: 0.881 (**f**).

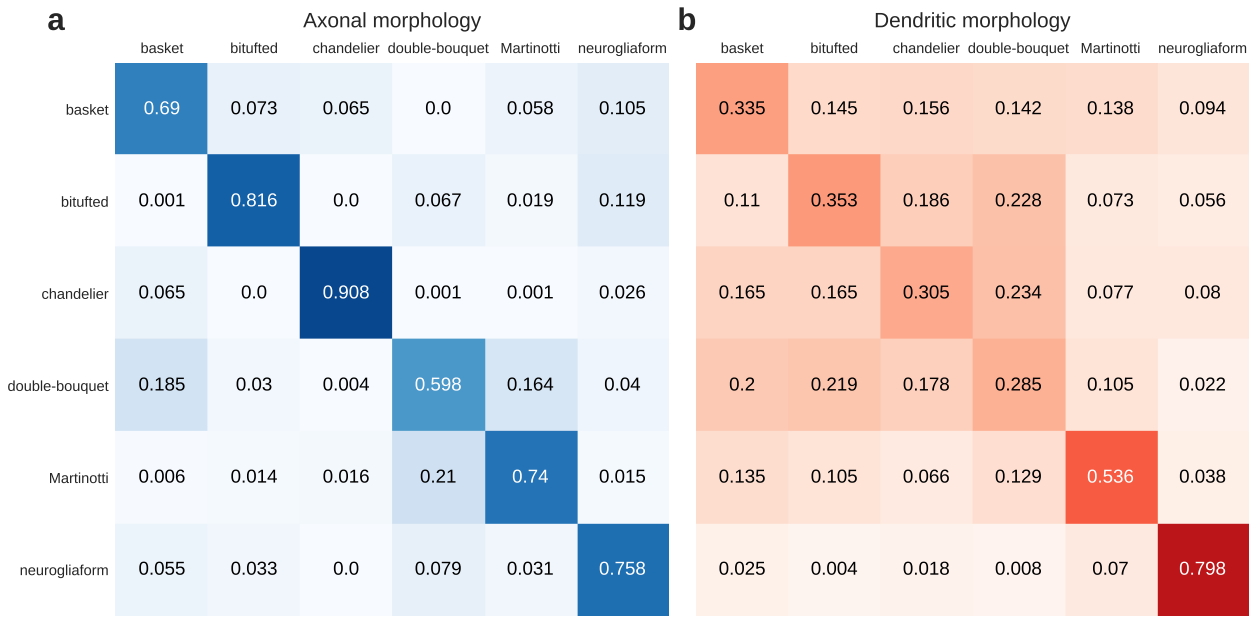

Figure S3: Classification by morphology of six interneuron types. a. Only axonal tree morphology, average F_1-score: 0.752. **b.** Only dendritic tree morphology, average F_1-score: 0.435.

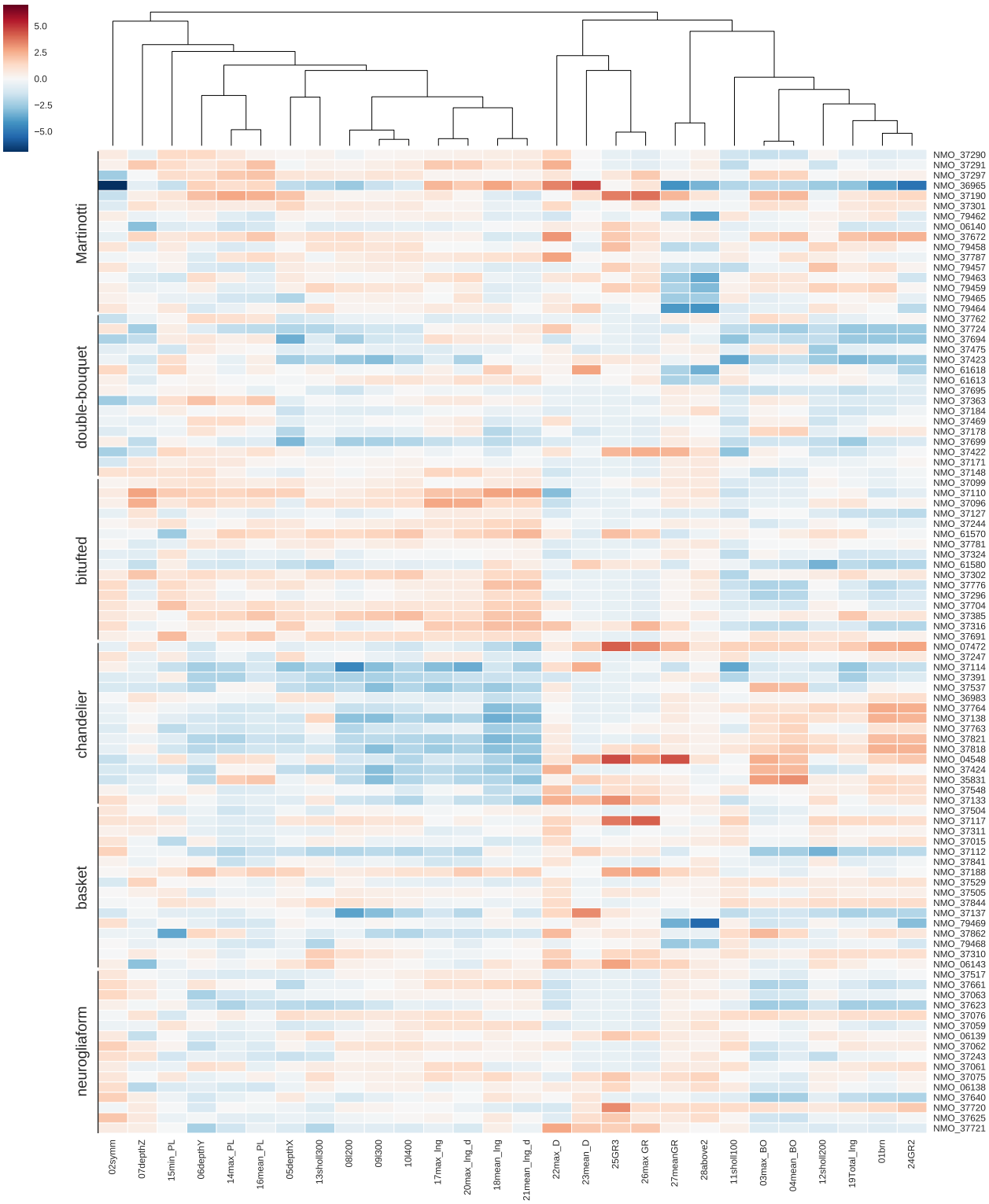

Figure S4: A heatmap comparing the distributions of morphological parameters. The parameters were transferred to z-score values. The *NeuroMorpho.Org* IDs are indicated for each neuron reconstruction on the right side, and the interneuron subtype is indicated on the left side. The columns are the 28 morphological parameters organized according to the above dendrogram.

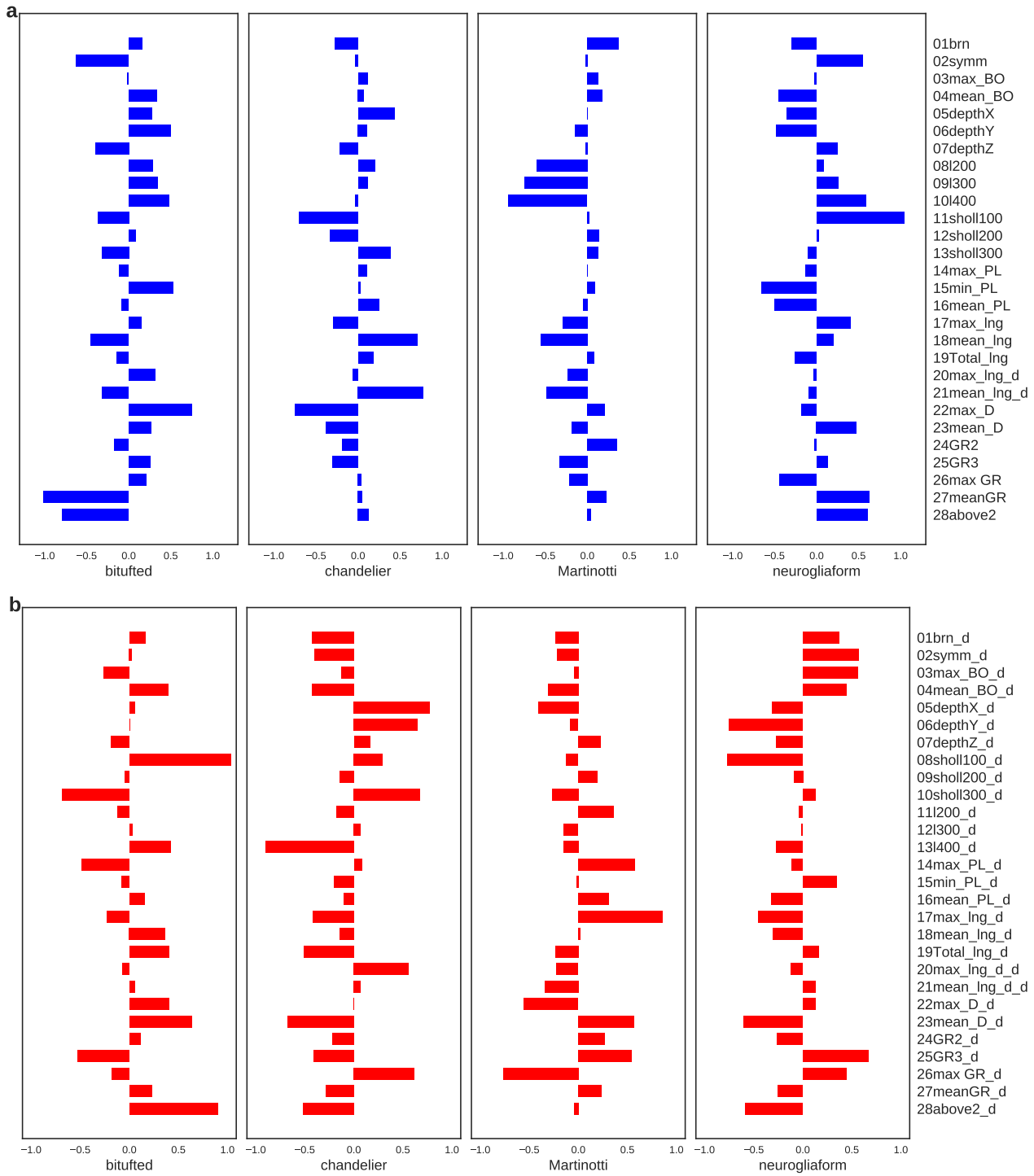

Figure S5: Logistic regression coefficients. The average of the logistic regression coefficients for the 1,000 repeats of the axonal (**a**) and dendritic (**b**) trees' morphology. Positive values indicate the significance of this feature for the specific interneuron type.

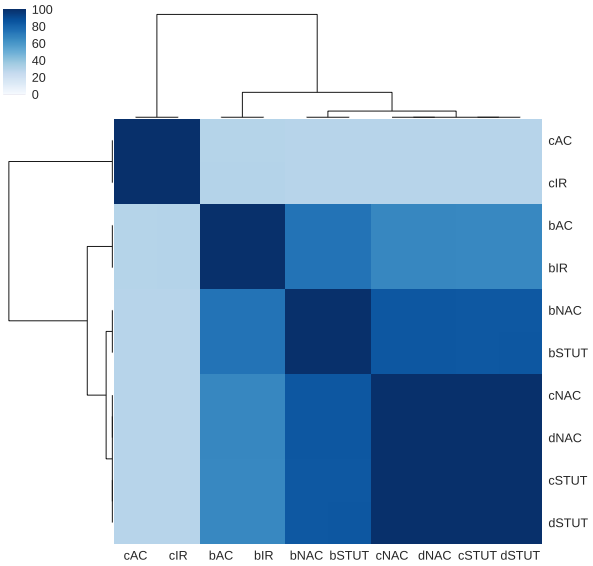

Figure S6: Comparison between 10 e-types from the BBP. A heatmap showing the similarity between all 10 interneuron e-types under current pulse frequencies of $100Hz, 200Hz, 300Hz$, and $400Hz$ in terms of firing pattern, in a basket cell (NMO_06143). In the original experiments conducted by BBP, an elongated current step was induced, resulting in significant differences between these 10 e-types. In our case, the soma was stimulated with strong current pulses, leading to very similar responses in several e-types. Hence, we chose to focus on four e-types: cAC, bAC, bNAC, and cNAC.

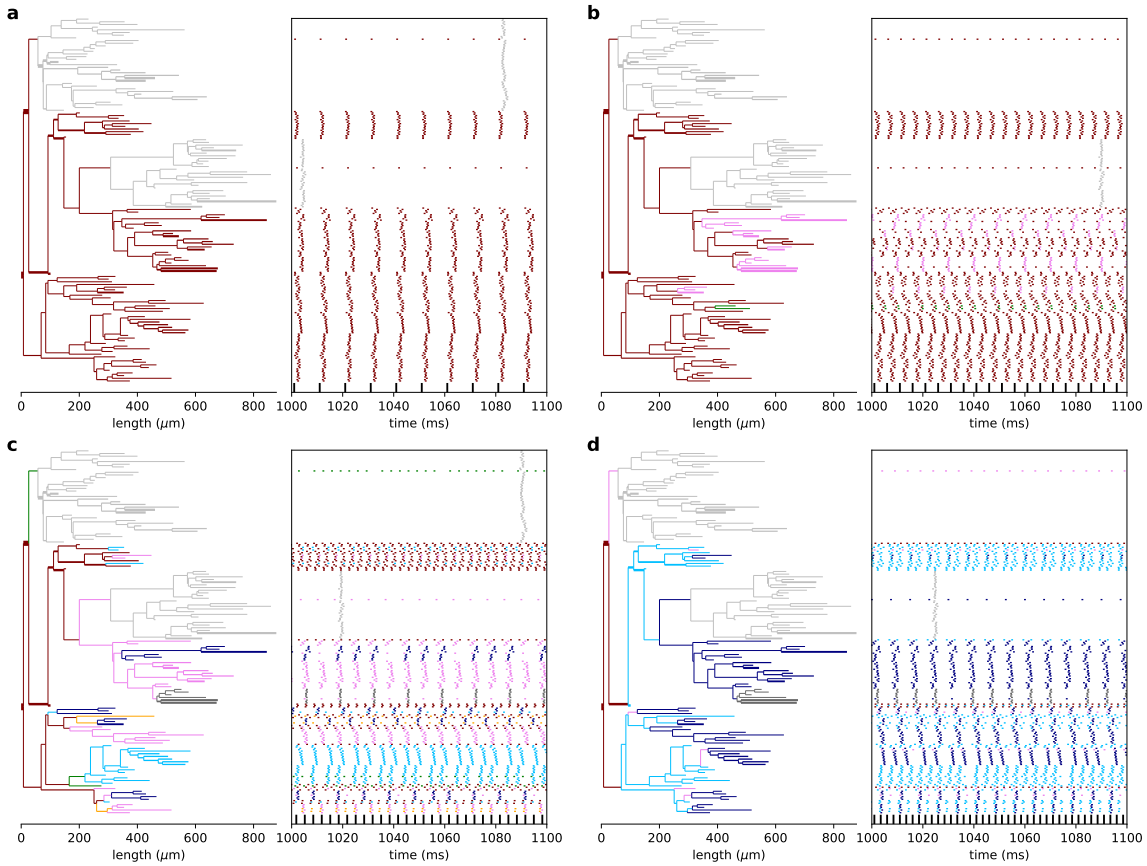

Figure S7: The response for varied stimulus frequencies. 'cAC' e-type. **a.** $100Hz$ **b.** $200Hz$ **c.** $300Hz$ **d.** $400Hz$. The line color indicates the fraction of spike train that propagates: maroon - 1, orange - 0.75, deep sky blue - 0.66, violet - 0.5, navy - 0.375, dim gray - 0.2, and silver - 0. The same neuron as in Fig. 3.

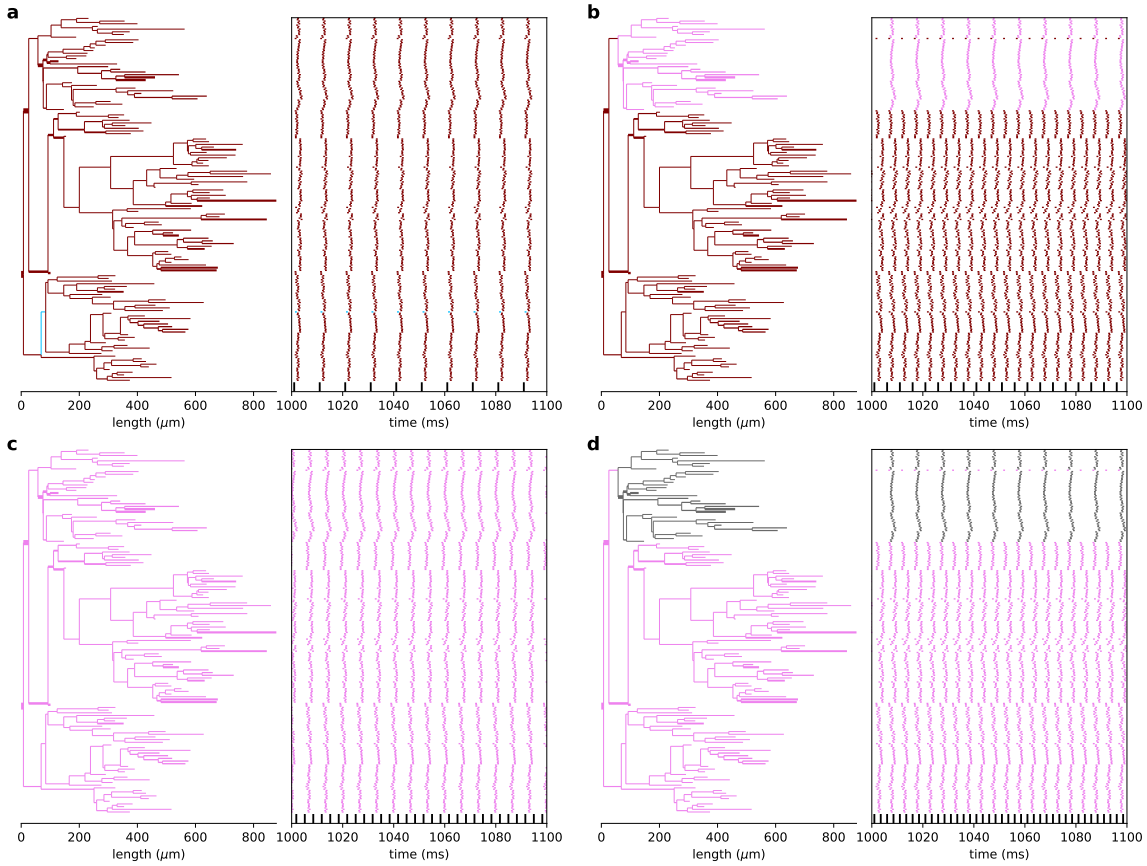

Figure S8: The response for varied stimulus frequencies. 'bAC' e-type. **a.** $100Hz$ **b.** $200Hz$ **c.** $300Hz$ **d.** $400Hz$.

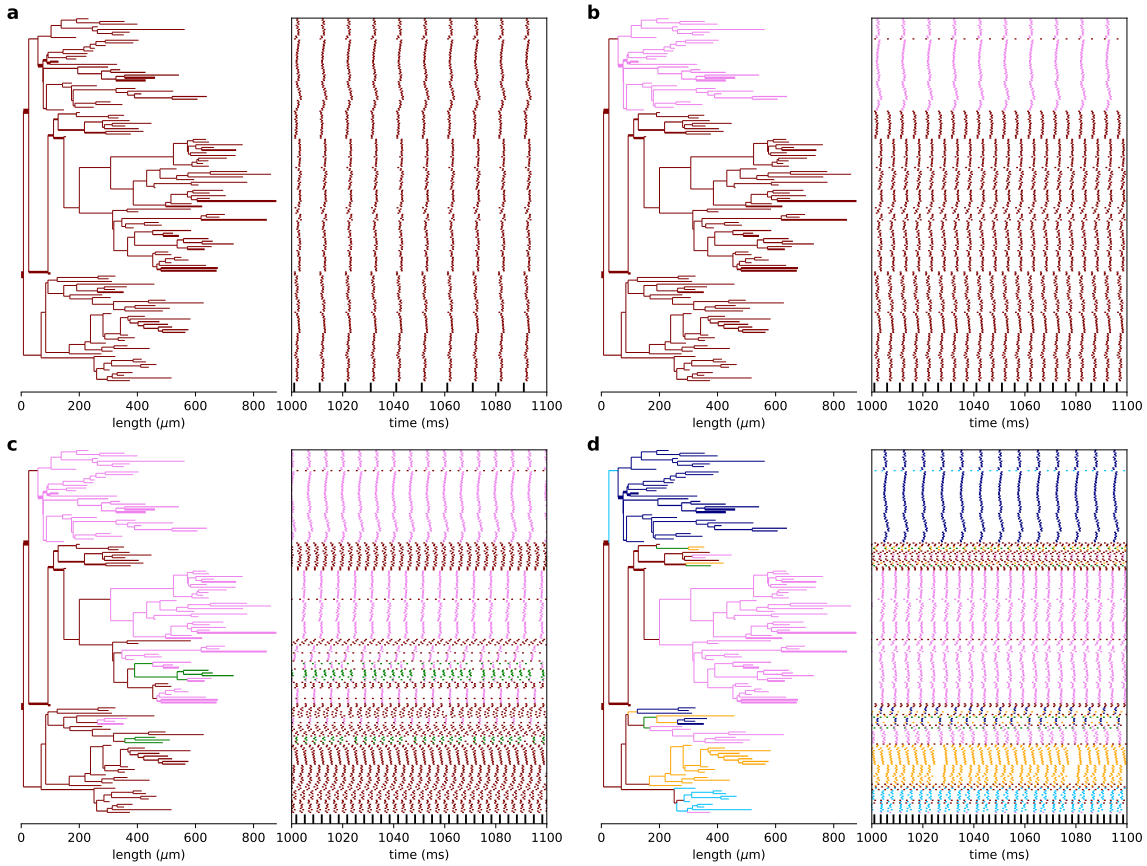

Figure S9: The response for varied stimulus frequencies. 'bNAC' e-type. **a.** $100Hz$ **b.** $200Hz$ **c.** $300Hz$ **d.** $400Hz$.

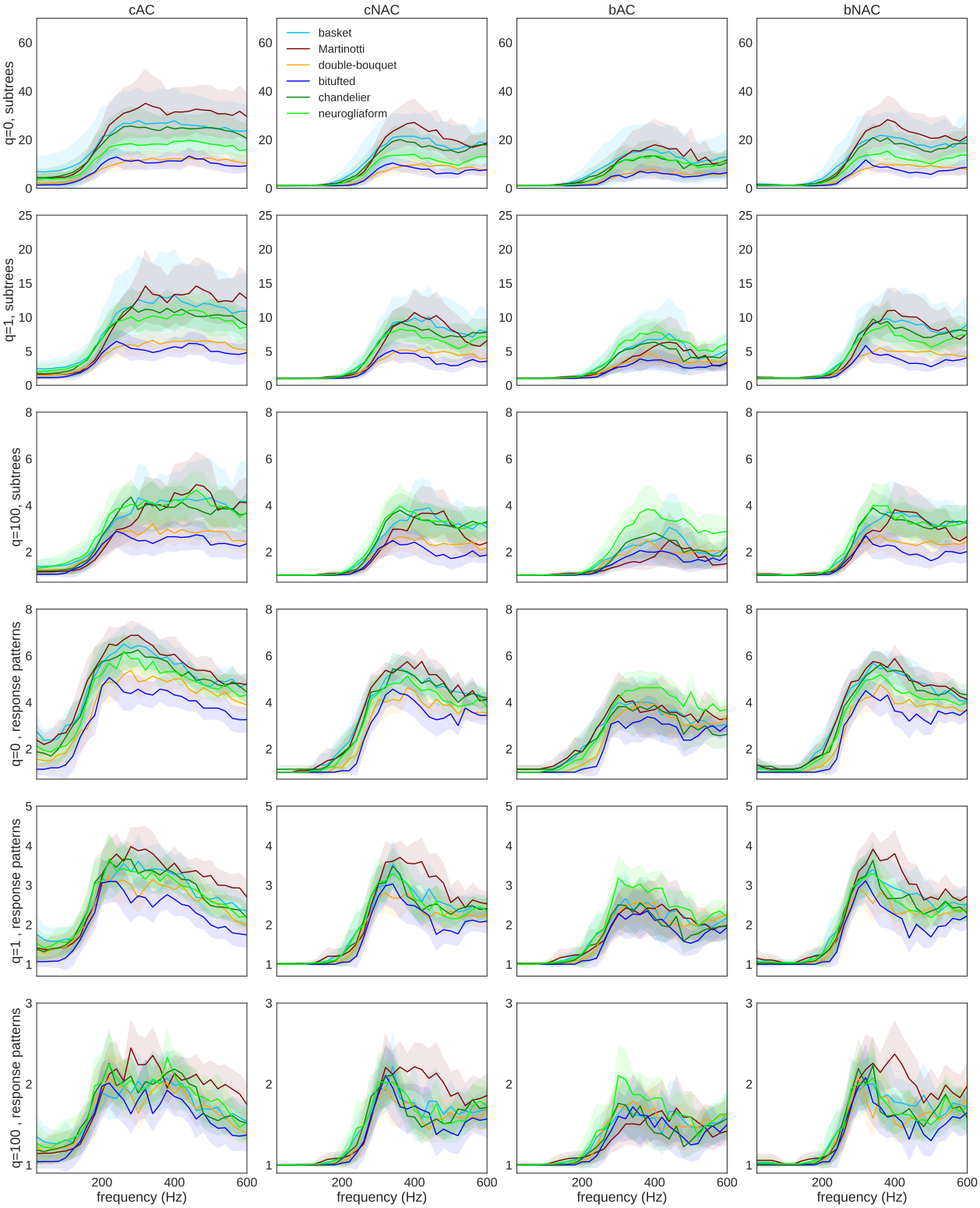

Figure S10: Mean of the diversity index at different frequencies. The shaded region represents one standard deviation. e-types: cAC, cNAC, bAC, and bNAC, for $q = 0, 1, 100$, for the number of subtrees and the number of branches for each type of response.

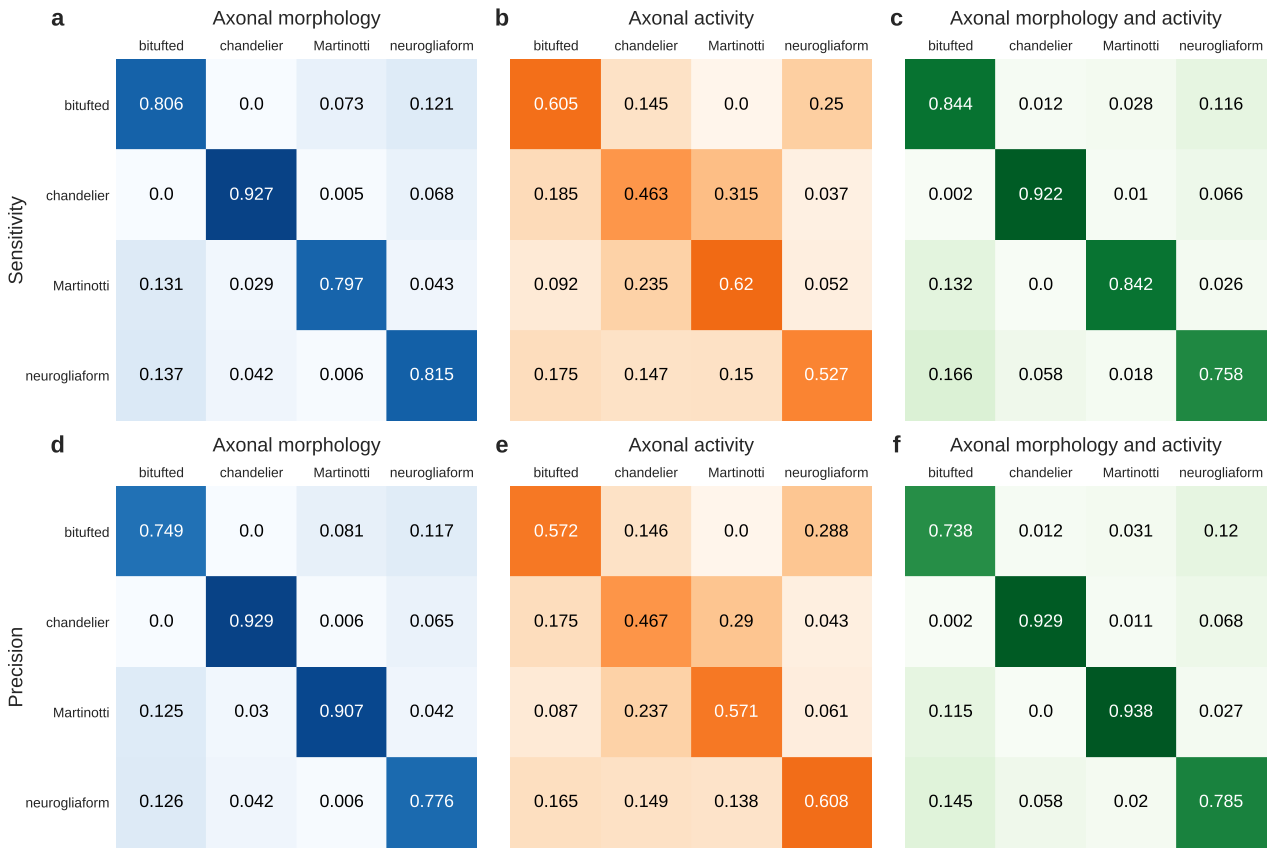

Figure S11: Classification by activity - sensitivity and precision. Only axon morphology, average sensitivity score: 0.836 (**a**), average precision score: 0.84 (**d**). Only activity, average sensitivity score: 0.554 (**b**), average precision score: 0.555 (**e**). Axon morphology and activity, average sensitivity score: 0.842 (**c**), average precision score: 0.847 (**f**). e-types: cNAC, cAC, bAC, and bNAC, $q = 0, 1, 100$.

Figure S12: Classification by the activity of six interneuron types. e-types: cNAC, cAC, bAC, and bNAC, $q = 0, 1, 100$, average F_1-score: 0.296.

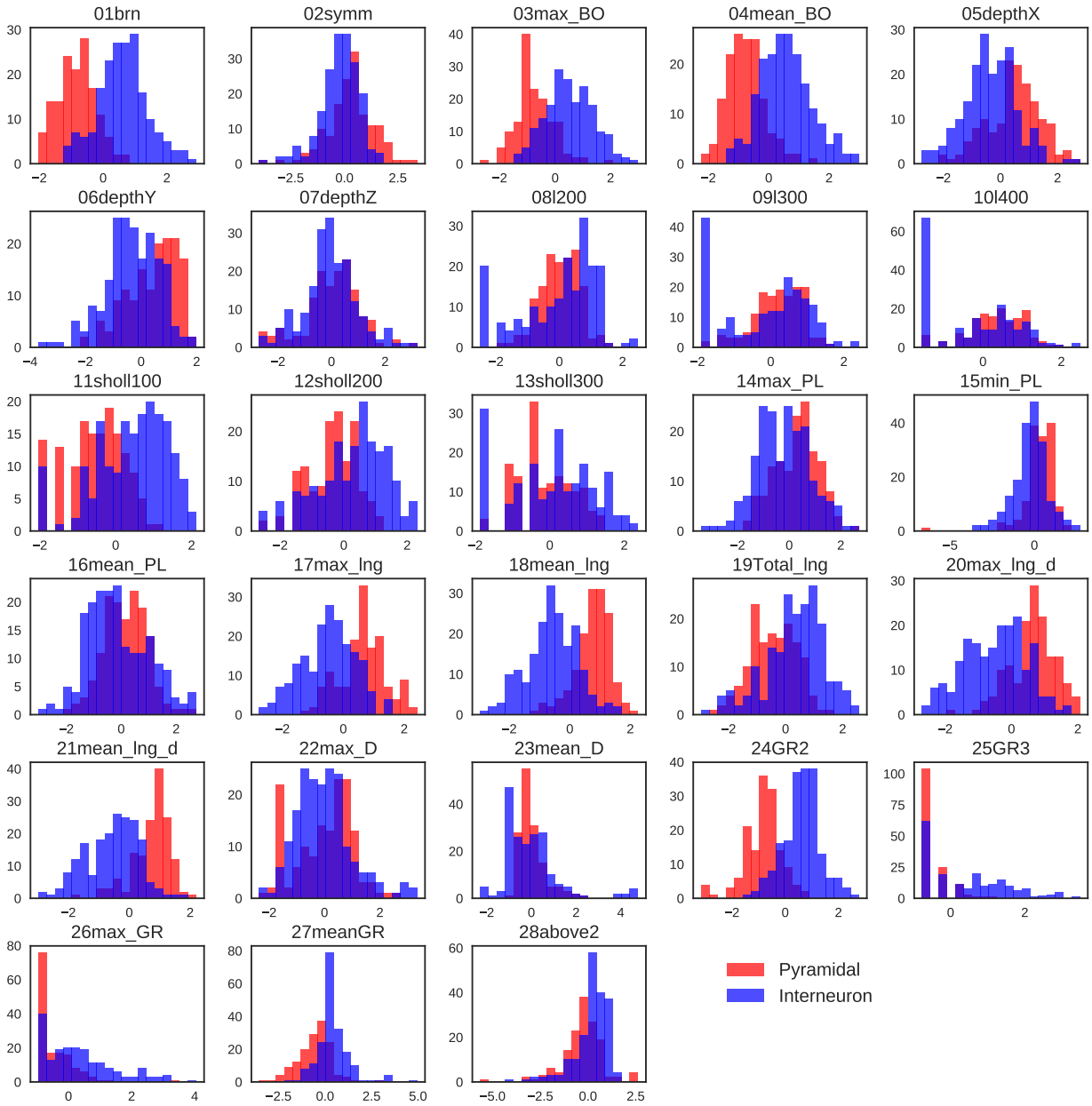

Figure S13: Histogram of the morphological features. The z-score of parameters that have been log-transformed is presented.

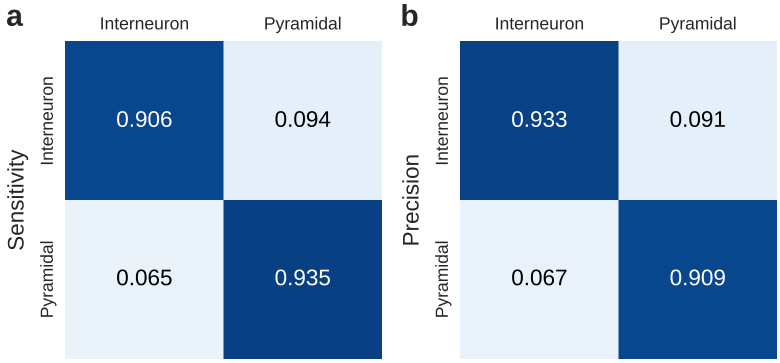

Figure S14: Classification by morphology. a. Sensitivity, average F_1-score: 0.921. **b.** Precision, average F_1-score: 0.921.

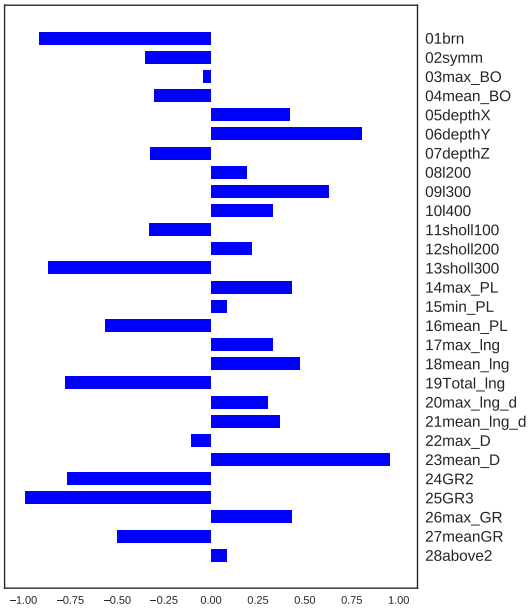

Figure S15: Logistic regression coefficients. Average of the logistic regression coefficients for 1,000 repeats. Positive values indicate significance in pyramidal cells, and negative values indicate significance in interneurons.

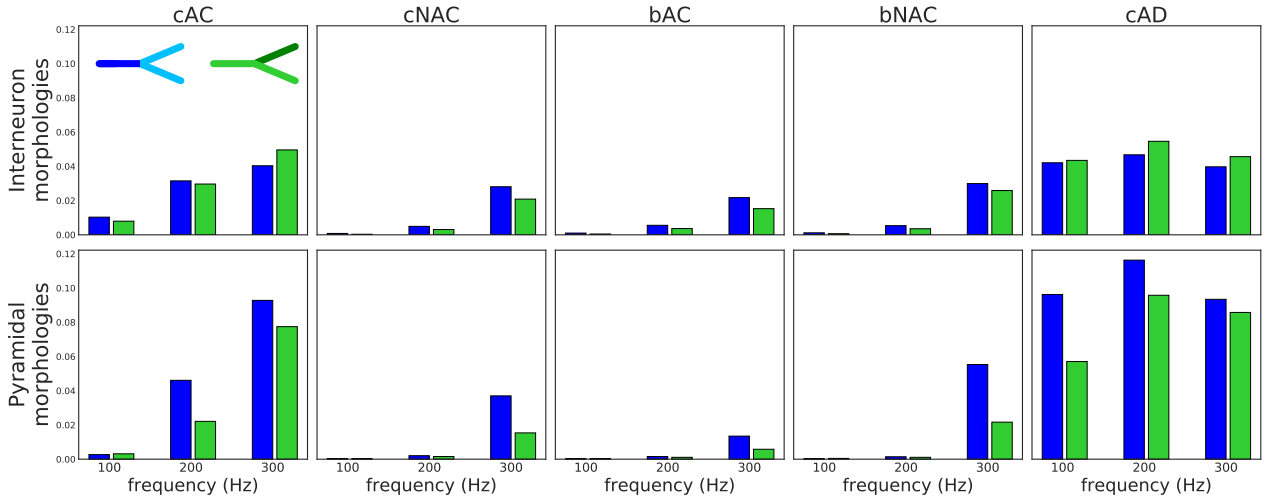

Figure S16: Symmetric and asymmetric responses at branching points. The fraction of modulated responses at branching points, for interneurons and pyramidal morphologies under various stimulus frequencies for five e-types. The upper frames show the simulation results of the 192 interneuron reconstructions, and the lower frames show the simulation results of 146 pyramidal reconstructions. Symmetric responses are in blue, and asymmetric responses are in green. The asymmetric states include situations where the firing pattern at the mother branch is the same or different from the firing pattern at one of the daughter branches. Interneuron morphologies with cAD e-type, and pyramidal morphologies with cAC, cNAC, bAC, and bNAC e-types are speculative and are not actual existing scenarios. We simulated these scenarios to examine the extent to which different activities are affected by morphology and by ion channels.